TNO Report

Date	29th August 2018
Author(s)	Karan S. Narayan
Copy no.	1
No. of copies	3
No. of pages	50
No. of appendices	2
Sponsor	Holst Centre
Project name	High Performance Batteries
Project number	

Lithium Metal Batteries

Mitigating Dendrite Formation

by

Karan Narayan

in partial fulfillment of the requirements for the degree of

Master of Science

in Sustainable Energy Technology

at the Delft University of Technology,

to be defended publicly on Wednesday August 29, 2018 at 02:00 PM.

Supervisor:	Prof. dr. ir. M. Wagemaker (TU Delft)
	Dr. Sandeep Unnikrishnan (TNO - Holst Centre)
Thesis committee:	Prof. dr. ir. M. Wagemaker
	Prof. dr. E. Kelder
	Prof. dr. A. Smets

This thesis is confidential and subject to a NDA

Abstract

Li-ion batteries are the electrochemical storage technology of choice today. But, commercial Li-ion batteries are approaching their maximum theoretical capacity. The major challenge in batteries today is to overcome the limits on energy and power densities, while maintaining safe operating conditions. A promising approach is the use of metallic lithium in batteries. Such Li-metal batteries are more energy dense than Li-ion batteries, but are also prone to failure due to the instability of Li metal. The most common pathway of battery failure involves the formation of lithium dendrites. They form when dead (unreactive) Li metal is deposited in the battery. This causes capacity loss and potential short-circuits, which then leads to overheating and thermal runway. This report aims to alleviate such issues through the use of (1) polymer electrolytes, which provide mechanical stability against dendrite formation (2) interfacial ZnO layers, which may assist in the efficient plating and stripping of Li metal required in a Li-metal battery. A PEO-LiTFSI electrolyte was developed and characterised. The conductivity was measured against temperature and pressure. It ranged between $3x10^{-4}S/cm$ at $60^{\circ}C$ to $3x10^{-6}S/cm$ at $60^{\circ}C$. No discernible effect of pressure on conductivity was found. The transference number of the electrolyte was also calculated to be 0.21. This was followed by the use of spatial ALD to deposit thin ZnO layers of $\sim 200nm$ thickness on copper substrates (which act as the current collector). The plating/stripping of Li metal with and without the ZnO was compared in a standard liquid electrolyte (1M $LiPF_6$ in EC/DMC). The performance was compared over 50 cycles at 3 different current densities. The ZnO layer improved the plating performance, particularly at high current densities. It also delayed the failure of the cell.

Acknowledgments

This thesis has, by some distance, been the most challenging academic endeavour of my life. I would never have come this far without the support of many others. The list of names are too numerous to mention, but I must give special thanks to:

1. **Michal Tulodzcieki**: My first thesis supervisor at TNO and the finest researcher I have met
2. **Marnix Wagemaker**: My thesis supervisor at TU Delft for giving an engineer the chance to work in the fundamental sciences
3. **Sandeep Unnikrishnan**: For his constant support and guidance through my thesis
4. **Lucas Haverkate**: For graciously taking up the additional responsibility of supervising me at the final stages of the project
5. **Ming Liu**: For his selfless inputs and suggestions on the development of experiments
6. **Andrea Bracesco**: For being an incisive critic and wonderful companion

Last but not the least, to my parents. Nothing I say here can convey the extent of my gratitude. For everything, thank you.

Karan S. Narayan
Delft, August 2018

Holst Centre

Holst Centre is an independent R&D centre that develops technologies for wireless autonomous sensor technologies and for flexible electronics, in an open innovation setting and in dedicated research trajectories. A key feature of Holst Centre is its partnership model with industry and academia based around shared roadmaps and programs. It is this kind of cross-fertilisation that enables Holst Centre to tune its scientific strategy to industrial needs.

Holst Centre was set up in 2005 by imec (Flanders, Belgium) and TNO (The Netherlands) and is supported by local, regional and national governments. It is named after Gilles Holst, a Dutch pioneer in Research and Development and first director of Philips Research. Located on High Tech Campus Eindhoven, Holst Centre benefits from, and contributes to, the state-of-the-art on-site facilities. Holst Centre has over 200 employees from some 28 nations and a commitment from over 40 industrial partners.

Research Focus

Combining expertise in wireless sensor technologies and flexible electronics under one roof puts Holst Centre in a unique position, in both domains as well as in the synergy between them.

Business Model

Due to the increasing complexity of products and systems, and accelerating progress in physics, life-sciences, materials, electronics, software, etc., R&D costs are growing faster than company revenues.

This is why the goal of open innovation is to share ideas, efforts, costs and risks, and to reduce time to market for new product generations. At Holst Centre, partners complement their own exclusive R&D with shared R&D, leveraging each other's talents and know-how in a well-structured and professional corporate R&D-like setting. Typically, Holst Centre results are shared on a non-exclusive basis between program partners according to customised agreements, tuned to each partner's needs and situation.

Whenever appropriate, Holst Centre also facilitates more dedicated research trajectories. We often do this to speed up the technology transfer and industrial uptake of results obtained in shared research, that have reached a higher technology readiness level. Also, this model helps in our collaborations with SMEs who typically have a shorter R&D horizon. For these collaborations, dedicated partnership and IP agreements are discussed with the companies involved.

Contents

List of Figures

List of Tables

1

Introduction

An overview of the available types of electrical energy storage technology is shown in Figure 1.1. This is called a Ragone chart (this example also indicates the stage of commercialisation). The gravimetric (per unit mass) power and energy densities are on the vertical and horizontal axes, respectively. Power is simply the rate of transfer of energy. This means that those technologies on the top left corner can deliver large amounts of energy relative to the time in which the energy is delivered, for a given mass. Those technologies in the bottom right corner can hold large amounts of energy, but only deliver a small portion of that energy in any given time. The ideal type of technology depends on the application considered: (1) delivering large amounts of energy in short bursts (e.g. capacitors) (2) storing large amounts of energy for sustained supply (e.g. grid-storage batteries).

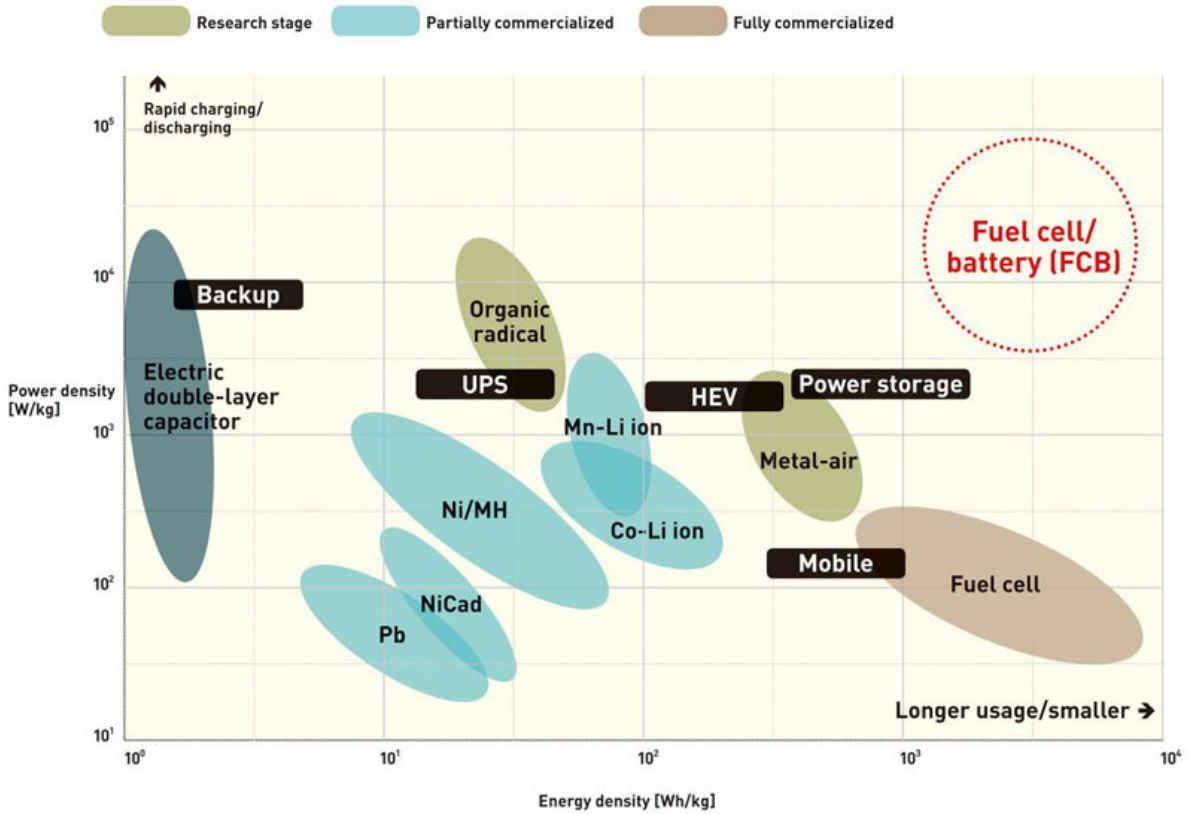

Figure 1.1: Ragone chart: storage technologies mapped according to energy and power capabilities. Source: [1]

The aim of the this research project is a technology that provides the best of both worlds. This can be viewed through the lens of a leading application in electrical storage technology: electric vehicles (EVs). EVs must have reasonably large energy storage capabilities so that they can drive long distances (ranges) on a single charge. But, they must also be capable of delivering relatively large amounts of energy in a short period of time, such as during acceleration on the freeway.

1.0.1. Power v/s Energy

The nature of electrical energy storage means that there is usually a compromise between the above objectives; if a device can reliably deliver a large amount of power, it usually cannot store a commensurately large amount of energy. This can often be explained by the internal chemistry. Delivering high power means that the internal reactions in the device must transfer a large amount of charge in a short period of time, i.e. they must be able to provide high currents (electric current = electric charge transferred/Time of transfer). This means that the chemical components of the device must have an easy pathway in which to interact and release energy. This may be achieved by: (1) using fine particles with high surface area that will provide more chances for the reactions to occur (2) increasing the voids or spaces between the particles so that the reactants and products can easily move in and out respectively. But, particles with larger surface areas are not an improvement if the extra area cannot be accessed. This access is limited by the available space around the particles. Increasing the space around the particles means that fewer of them can be packed in any given volume. This reduces the energy capacity since there is less active material.

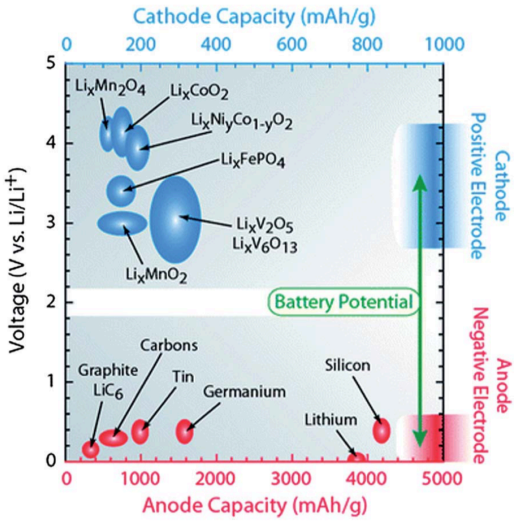

Figure 1.2: Capacity, and voltage versus Li/Li+ for different electrode materials. Source: [2]

There may be 2 ways to resolve this issue: (1) make the components of the device more dense so that more mass can be packed into the same volume (2) use chemical substances which can deliver a large amount of energy per unit mass. The first approach leads to the idea of solid-state batteries, in which the electrolyte is a solid instead of a gel/liquid. The second approach leads to the idea of using pure lithium (Li) metal as the anode in the battery, instead of Li compounds. Currently, Li ions from the electrolyte are intercalated into electrode materials (e.g. anode - C, Si & cathode - MnO_2, $FePO_4$) to form Li complexes (e.g. LiC_6, Li_4Si $LiMnO_2$, $LiFePO_4$). The energy capacities of these electrodes is shown in figure 1.2 Combining the two approaches would result in a solid-state Li metal battery. This is the end-goal of this research path.

1.0.2. Lithium Metal Anode

Li metal has a high capacity of $3860mAh/g$, low density of $0.59g/cm^3$ and at $-3.04V$ also has the lowest negative potential versus the standard hydrogen electrode (SHE) [5]. In fact, Li metal batteries

were used commercially even before Sony brought Li-ion batteries to the mass market. They were primary batteries (not rechargeable) and were quickly discontinued after explosions and fires began to be reported. Li is very volatile for the same reasons that it is energy dense - it has a strong tendency to react to form compounds, releasing energy in the process. The use of Li metal as the anode also leads to infinite volume change during the Li plating/stripping cycle. since there is no matrix inside which the Li can be deposited (in an intercalation anode, the matrix of the anode material swells on intercalation of ions - this swelling is the volume change). This creates large mechanical stresses in the cell. For the same reason, carbon (in the form of graphite or graphene) is preferred to silicon as the intercalation anode in Li-ion cells [16]. While Si has a capacity of $4200mAh/g$ (v/s $372mAh/g$ for C), it expands by up to 400% (v/s 10%) during the cycling process [7].

1.0.3. Dendrites

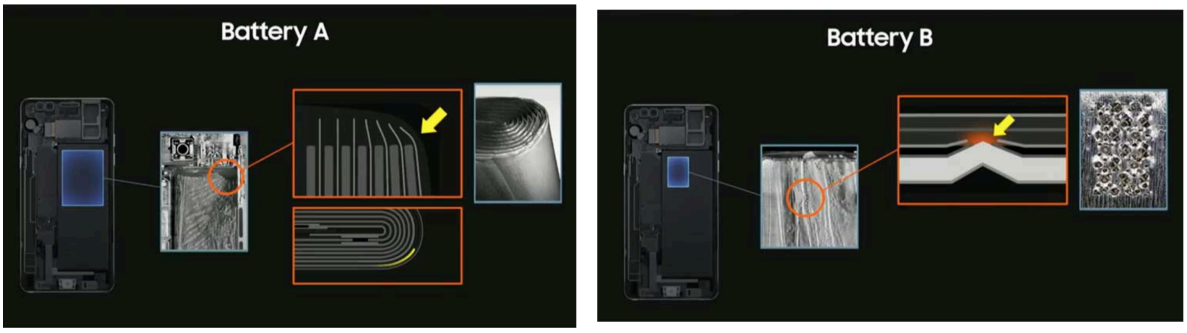

(a) (b)

Figure 1.3: Two independent manufacturing defects that led to separator failures. Source: [3]

However, using Li-ion batteries carry their own risks. This is in large part due to the volatility of the liquid/gel electrolyte, which when heated could produce vapours, increase the pressure in the battery and eventually cause it to explode. Such heating can occur due to an internal short-circuit, which was sharply illustrated by the Samsung Galaxy Note 7. Two different manufacturing defects caused punctures in the separator, as illustrated in figure 1.3. In (a) electrodes were deformed due to poor pouch design, and in (b) burrs up to $80\mu m$ deep were caused by inconsistent welding.These punctures eventually led the electrodes to contact, thus causing the cell to short-circuit and the battery to explode.

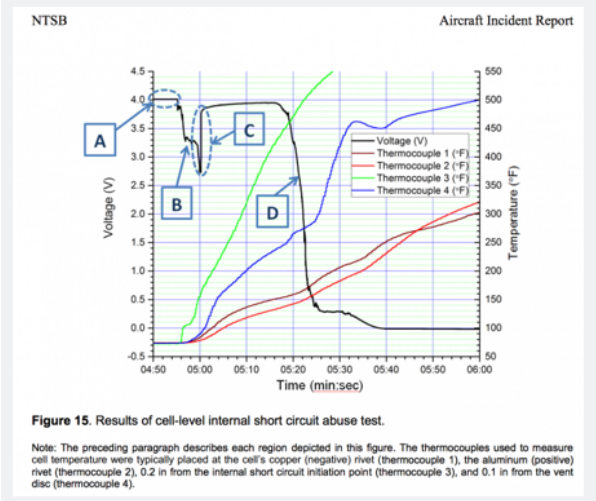

Figure 1.4: Results of tests run by the NTSB depicting the origins of thermal runaway in Boeing 787. Source: [4]

Even before the Note 7, there were well-reported incidents pertaining Li-ion batteries. A Japan Airlines Boeing 787 aircraft caught fire at the runway in Boston in 2013. The National Transportation and Safety Board (NTSB) identified the Li-ion batteries used in the auxiliary power unit (APU) as the source of the fire [4]. This was closely followed by another incident on a All Nippon Airways 787 in Japan where the main battery system caught fire. In both cases, the cause was identified as ”thermal runaway” - a self-sustaining series of chemical reactions that successively generate more heat to the point where the battery catches fire. The root cause was identified as the formation of Li dendrites in the batteries, which led to internal short-circuits. The dendrites formed on wrinkles in the electrolyte material when it was being wound - a serious manufacturing defect. The nature of such dendrites will be discussed in the next chapter.

1.0.4. Research Questions

Solid-state batteries therefore can potentially: (1) decrease the size of the batteries by using solids, which are more mass dense (2) increase the energy output of the batteries by using Limetal, which is more energy dense and (3) increase the safety of the batteries, by removing the volatile liquid electrolyte. The third benefit, however, could be offset by the second due the volatility of Limetal. Thus, among the major research questions in batteries today is: how do we use Li metal in a battery without compromising safety? The joint research project between TU Delft and TNO aims to resolve the question and develop a working, solid-state Li metal battery. This report investigates 2 approaches to this end:

- Using solid-state polymer electrolytes. These materials can have very good mechanical, chemical and thermal stability. The drawback, however, is their relatively low ionic conductivity. In order to approach the conductivities of liquid electrolytes, modificications to the polymer are required. This report uses a Li salt in a semi-crytsalline polymer to this end.
- Using an interfacial layer to improve the plating/stripping performance of Li anodes. The hostless nature of the anode combined with the instability of Li metal leads to inhomogeneous depositions that provide the base for dendrite formation.

These approaches yield the following research questions that this thesis aims to answer:

1. **What type of polymer electrolyte could have the requisite mechanical, electrical and chemical properties?**
2. **How do you develop this electrolyte in a scalable, reproducible manner?**
3. **How does the developed electrolyte behave electrochemically under different operating conditions?**
4. **What type of interfacial layer could aid the Li plating/stripping process?**
5. **How can this interfacial layer be developed?**
6. **How does the performance of the layer change under different operating conditions?**
7. **Does this layer achieve the aim of improving the plating/stripping performance?**

2

Literature Review

This chapter will attempt to lay the groundwork for the experimental investigation that follows. The aim is to determine what the underlying mechanisms in dendrite formation are and why the measures chosen in this thesis may help alleviate the issues. It is also the intention to choose specific candidates for the polymer, Li salt and the interfacial layer which will be investigated.

2.1. Dendrites

It was mentioned in the previous section that Li metal was used as a primary battery, before secondary (rechargeable) Li-ion batteries were introduced by Sony. It was also mentioned that the Galaxy Note 7 failed due to punctures that led to a short-circuit. Although these punctures were caused by manufacturing errors and not the internal chemistry of the battery, using Li metal in a secondary battery increases the risk of creating such punctures. This is because they increase the likelihood of the formation of what are known as dendrites. As the name suggests, dendrites are tree like structures that are made of deposited Li metal. These dendrites can be formed even when Li metal is not initially present in the battery. Instead, Li-ions initially present in the electrolyte may get deposited as Li metal over multiple cycles. This may happen while using either liquid or solid electrolytes.

These dendrites could then internally short the battery, if they cross the length of the battery through the separator. The separator in a battery is meant to safeguard against internal short-circuits by creating a physical barrier between the electrodes. But, it is often made extremely thin to save space and weight. It, after all, provides no utility in the flow of energy. The failure of the separator due to poor battery design and incorrect manufacturing (driven by rushed scheduling) was identified as the primary cause of the Note 7 disaster. [17].

2.1.1. Formation

The exact mechanisms for the formation of Li dendrites are still unknown. This is also because their process of formation depends on the chemical components of the cell. The key points that need to be researched to arrive at the mechanisms are [7]:

1. **Solid Electrolyte Interface (SEI)**
    - A physical layer formed by the products of parasitic reactions between the electrode and electrolyte
    - Serves as a passivating layer that improves the electrochemical stability of the cell, and consequently the cycling performance
    - Mechanisms of formation and Li-ion migration through the interface is not yet well established

2. **Li-ion transfer and reaction nature**
    - Generally known that unstable i.e., heterogeneous Li deposition leads to dendrite formation
    - Higher current density & number of cycles increase likelihood of dendrite formation
    - Relationship between these variables and dendrite formation is not yet well established

The formation of Li dendrites is often studied comparatively to the aqueous electrodeposition of copper [5]. The scheme of processes is explained here: when a current flows through the cell, the cations flow to the cathode and get reduced. The anions, however, flow to the anode but do not engage in electrochemical reactions. The cations then tend to flow to regions of larger anion concentration to preserve electroneutrality. The neutral salt concentration (concentrations of cations + anions) tends to obey a diffusion limited equation. If the current is above this diffusion limit, the salt concentration vanishes as one approaches the electrode surface since the cations cannot compensate for the excess anions fast enough. This inhibits electrochemical reactions at the electrodes and renders further electroplating of the cations at the cathode unstable.

This mechanism has been studied visually using a capillary cell. The results are shown in figure 2.1. The voltage responses at the fixed current density of $2.61 mA/cm^2$ are in b. In the figures 2.1 c-g, the onset of dendrites is indicated in figure 2.1 e. The possible theoretical explanation is also shown graphically in figure 2.1 h.

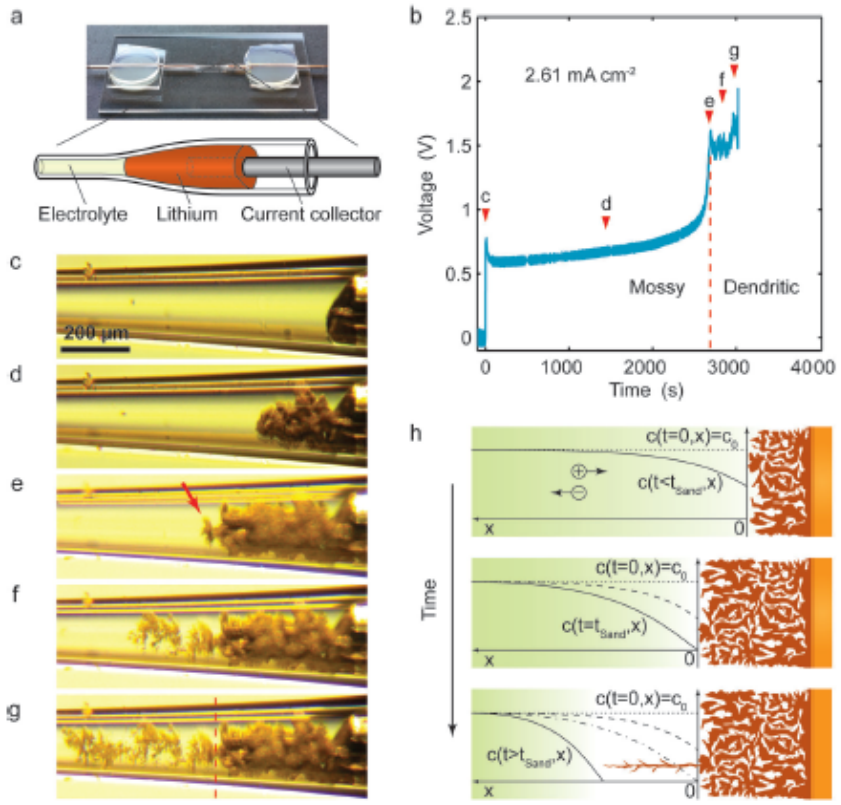

Figure 2.1: The formation of Li dendrites in a capillary cell. Source: [5]

The time that it takes for these processes to occur depends on the individual characteristics of the cell and is known as Sand's time. After this point in time, the few available cations preferentially deposit on outgrowths from the electrode surface, instead of on the electrode itself. These outgrowths grow at the same rate as the bulk anions, to maintain electroneutrality. The equation for Sand's time is:

$$t_{Sand} = \pi D_{app} \frac{(z_c c_o F)^2}{4(J t_a)^2} \tag{2.1}$$

where z_c is the charge number of the cation, c_o is the bulk salt concentration, F is Faraday's constant, J is the current density and t_a is the transference number of the anions ($= 1 - t_{Li^+}$).

The first reaction-limited mechanism causes the typically random formation of mossy Li from the roots. At the microscopic scale, the moss consist of small whiskers. Due to the formation of the SEI, Li develops these whiskers which are individually passivated from the electrolyte. Therefore, as it spreads into the electrolyte, the whiskers remain separately protected and the moss thickens. At the limiting time, the dendrites spike outwards from the tips of these whiskers. Now the second, diffusion-limited mechanism takes over. In comparison, copper electrodeposits uniformly and compactly.

In cells with Li anodes and polymer electrolytes, the dendrite formation time tends to scale with current as predicted by the equation above [5]. But, the currents at which it occurs is much lower than predicted values. This occurs even in cells with liquid electrolytes, but at relatively higher currents. Nevertheless, it appears from the morphology and dynamics that the shift from reaction-limited growth to transport-limited growth is what brings the onset of dendrites.

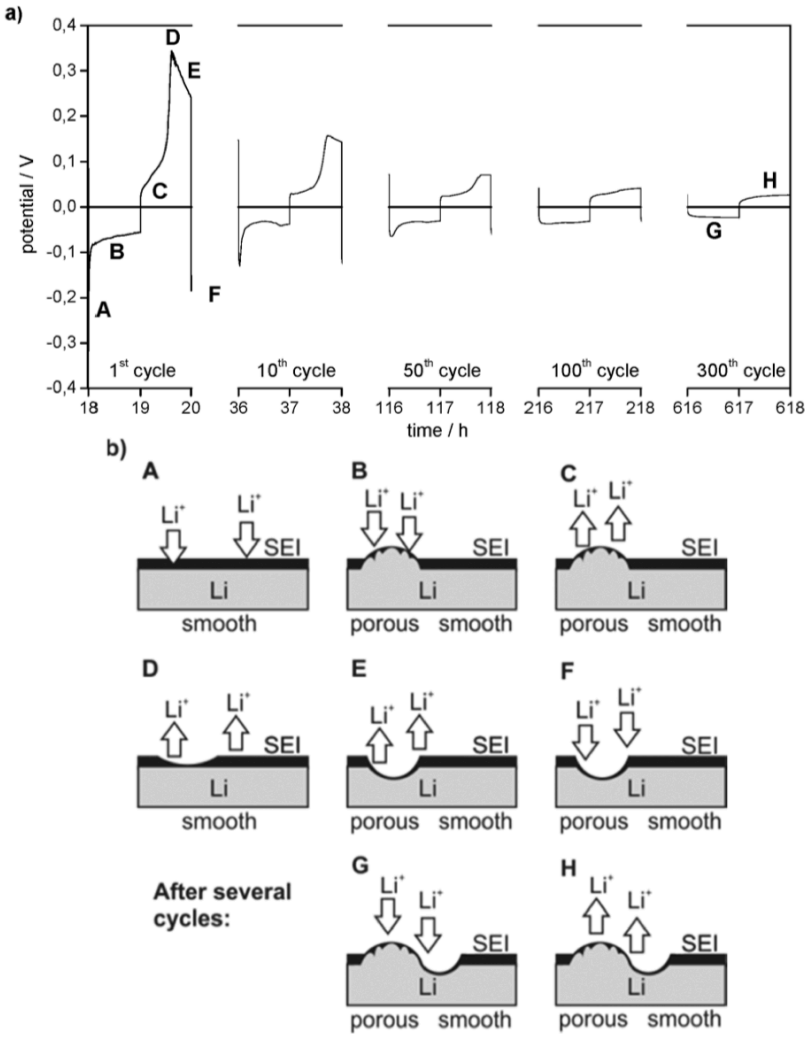

Figure 2.2: Changing overpotentials in the cell as dendrite formation occurs. Source: [6]

The formation of dendrites are also visible through changing overpotentials in the voltage plot of the cell. Initially, the overpotentials are rather high as deposition must occur on fresh Li which provides a resistive surface. However, once nucleation sites have been formed on this Li, there is larger surface area upon which deposition can occur. As the the surface becomes non-uniform, the current distribution

also becomes non-homogeneous leading to preferential local Li deposition. This brings the onset of dendrite formation. These self amplifying effects are shown schematically in figure 2.2:

2.1.2. Adverse effects

The most significant adverse effects that stem from dendrite formation are summarised using a schematic in figure 2.3, and elaborated on thereafter.

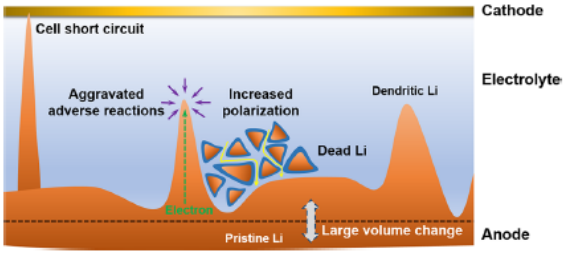

Figure 2.3: Significant issues caused by dendrite formation. Source: [7]

1. **Short circuit**
   - Dendrites can penetrate the separator and short the cell internally
   - This releases heat and could cause thermal runway - a chain reaction of sorts that leads to progressively higher temperatures
   - This in turn can lead to electrolyte combustion and cell explosion
2. **Parasitic reactions**
   - The dendrites provide increased Li surface area upon which reactions can occur
   - This leads to irreversible consumption of both the anode and the electrolyte
   - This decreases capacity and Coulombic efficiency
3. **Evolution of dead Li**
   - The aforementioned parasitic reactions caused further dendritic growth which is now wrapped in an SEI itself
   - This is inaccessible to current collectors and electrons and thus cannot participate in the Faradaic reactions of the cell
   - This unreactive Li is called 'dead' Li
4. **Polarisation**
   - The formation of dendrites occurs in an inhomogeneous fashion
   - This leads to a porous and uneven structure in the Li anode with the presence of dead Li
   - This increases the diffusion pathway and resistance of the Li ions and electrons, thus increasing overpotentials and decreasing energy efficiency
5. **Volume change**
   - Li anode would be hostless i.e., there is no matrix to strip/plate Li^+ ions
   - The volume change during this plating and stripping is thus, infinite ($Si = 400\%$, $C = 10\%$)
   - Dendrite exacerbates this issue by causing porosity, which makes the volume change even sharper

2.1.3. Solution approaches

It is generally accepted that dendrite formation is an unavoidable consequence when Li is used in a battery over multiple cycles. The current research approach is one of containment and management. This can be done either by: (1) preventing preferential nucleation of Li into sites which then leads to dendrite formation (2) suppressing further growth of Li dendrites once they have been formed. To this end, 4 strategies can be identified to mitigate the effects of dendrite formation:

Figure 2.4: Strategies to deal with dendrite formation. Source: [7]

1. LiX **alloy**
   - Decreased chance of dendrite formation because Li is present as ions and not metal
   - Unstable for long term use because of large volume changes during charge-discharge cycles
   - Carbon (graphite) alloy is the most successful solution so far, but decreases capacity by 90% compared to Li metal
2. Li **metal/electrolyte/interface modification**
   - Formation of SEI in non-aqueous electrolytes stabilises the Li metal somewhat
   - Additives are used to tune and optimise the performance of the SEI film
   - Functionality of film decreases through repeated Li plating/stripping
3. **Solid-state electrolyte**
   - These electrolytes have $> 2x$ the shear modulus of Li; they can suppress dendrites
   - They are also safer than liquid electrolytes because they are not flammable
   - But, their conductivity is 2-3 orders of magnitude lower than liquid electrolytes
4. **Structured anode design**
   - Nanotechnology is used to create matrix for Li plating/stripping
   - Half-cell have achieved up to 99.8% Coulombic efficiency over 200 cycles
   - More work is required to reach targets of $1000+$ cycles

The approach of this thesis project was jointly determined by the Holst Centre and TU Delft. Solid-state polymer electrolytes will be investigated for their feasibility. Moreover, the effect of study modified interfaces at the anode side will be studied. In particular, the approach of using thin deposited layers, instead of coatings, is a burgeoning field of research.

2.2. Polymer Electrolytes

There are broadly 2 categories of solid-state electrolyte: (1) ceramic (2) polymer. Both types have stability issues against Li and air. Polymer electrolytes, however, have the following advantages compared to ceramics: (1) higher elasticity (2) good mechanical strength (3) easier to process [18]. These make them particularly suitable for thin-film batteries that can be produced in a scalable fashion. The primary issue with polymer electrolytes are their low conductivity at room temperature. The highest reported values are in the order of $10^{-5} S/cm$ [19]. This a full 2 orders of magnitude lower than liquid electrolytes. It also at least 1 order of magnitude lower than the recommendation by the likes of Goodenough (a pioneer in Li-ion batteries).These relative merits are represented in figure 2.5

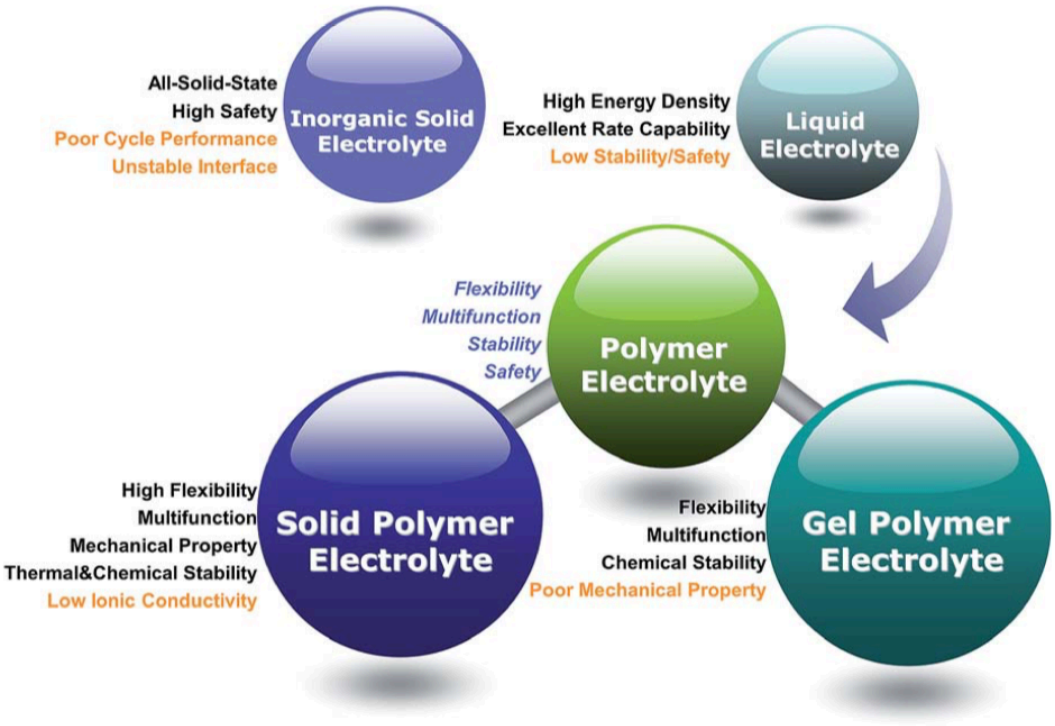

Figure 2.5: Comparison of electrolyte types for Li batteries. Source: [8]

The polymer electrolyte consists of a polymer matrix and Li salt. The general requirements for the polymer matrix are that: (1) it contains a polar group that can easily solvate the Li cation from the salt (2) and a low hindrance to bond rotation [20]. Nearly all candidates contain a strongly electronegative element (e.g. Cl, O, N). These groups provide sites upon which the Li cation can bond to the polymer backbone. The presence of these element would also result in intramolecular hydrogen bond formation, which can enhance the physio-chemical properties of the material.

2.2.1. Polyethylene Oxide (PEO)

Polyethylene oxide (PEO) has flexible chains with a high donor number for Li cations i.e., they can solvate a large number of Li cations. In addition, it also has a high dielectric strength which increases the strength of electric field across the electrolyte, and thus the voltage it can hold. It also has a high degree of segmental motion, which is important since it acts as the solvent in a solid-polymer electrolyte cell [19]. But it only has medium basicity; since Li cations require electron donors to form chemical bonds a higher basicity (electron donating tendency) is beneficial to stable bond formation.

Figure 2.6 displays how PEO tend to be semi-crystalline i.e., crystalline and amorphous phases tend to co-exist in the structure. It is well-known that the amorphous phase is largely responsible for the conduction in polymer electrolytes [20]. The segmental motion allows the solvated cation to hop between sites in the polymer matrix, and thus enabling conduction. This is shown schematically in

figure 2.7

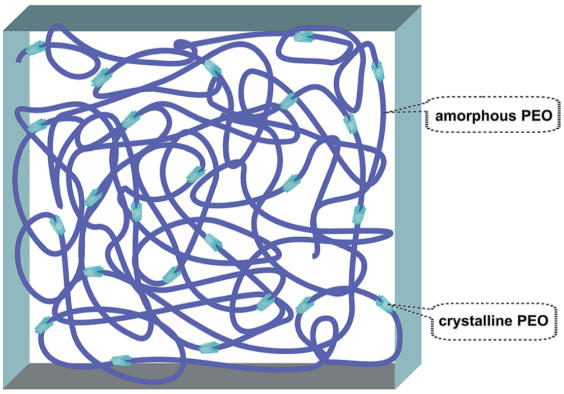

Figure 2.6: Crystalline and amorphous segments in PEO. Source: [8]

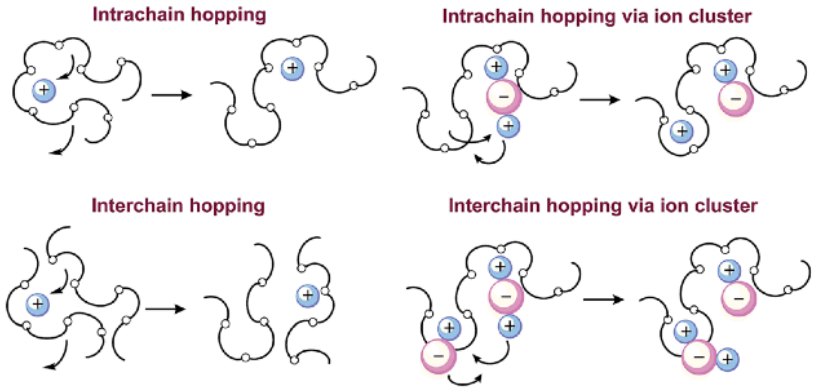

Figure 2.7: Ion transport in PEO. Source: [8]

2.2.2. Lithium bis(trifluoromethanesulfonyl)imide (LiTFSI)

For the Li salt, it is preferable to have a larger anion with a well-delocalised charge and low basicity. The addition of the salt also tends to decrease the crystallinity of the polymer matrix, thus aiding the requisite segmental motion. $LiTFSI$ has a strong electron withdrawing group ($-SO_2 - N - SO_2$) which results in strong dissociation. It also has high thermal, chemical and electrochemical stability. In addition, the $TFSI^-$ group is flexible and mobile. As a result conductivity values of up to $10^{-5} S/cm$ have been obtained using PEO-LiTFSI complexes.

An option to increase the ionic conductivity is to use room temperature ionic liquids (RTIL). These are salts with low melting points that are in the liquid state at room temperature. They are usually non-flammable and non-volatile. They also have high ionic conductivity and high thermal and chemical stability. However, when they were used in this project, the mechanical properties degraded to the extent that free-standing thin films could not be formed. Thus, they were abandoned in favour of the plasticiser succinonitrile (SN).

Since the amorphous regions are predominantly responsible for ionic conduction in polymer electrolytes, suppressing the crystallinity using plasticisers is another option to increase conductivity. Most commonly, liquid plasticisers such as organic solvents are used. But, they result in severe degradation of mechanical properties and thus the film forming ability. They also reduce the quality of the interfacial contact with the electrodes [8]. A more promising approach has been to use plastic crystals such as succinonitrile (SN). Aside from suppressing the crystallinity, it has also been found to assist in the ionisation of the Li salt. The development and testing of thin film polymer electrolytes using PEO and

$LiTFSI$ is the 1st aim of this thesis project.

2.3. Interfacial Layers

It was mentioned earlier that one of the routes for dendrite formation is the preferential nucleation of Li on certain sites. This leads to heterogeneous deposition of the ions as metals, which over the course of many cycles propagate as dendrites. A solution seems to be to create a lithiophilic matrix within which the Li has no preferential sites for deposition. An example of such a 3D porous matrix is displayed in figure 2.8. Instead it deposits uniformly inside the matrix due to the presence of pathways for favourable reaction mechanisms.

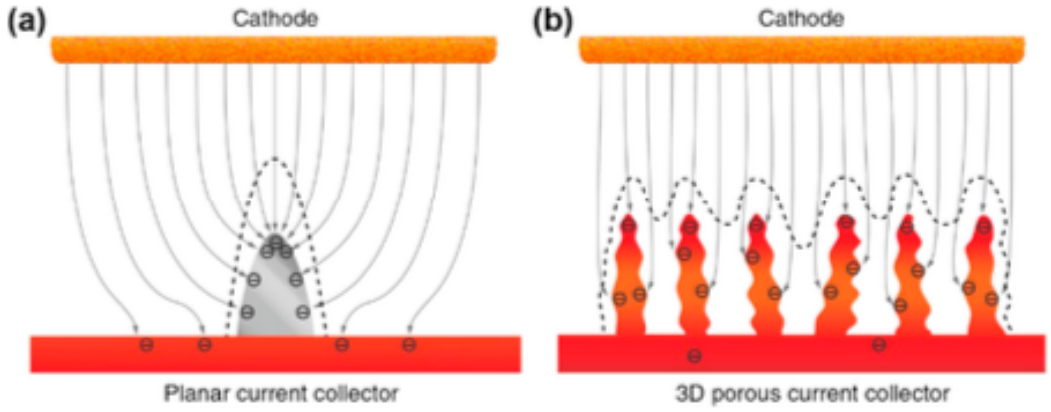

Figure 2.8: A 3D porous current collector matrix for uniform plating/stripping of Li metal. Source: [7]

2.3.1. Zinc Oxide

A study in this regard was conducted using a polymeric matrix formed from polyimide, onto which a ZnO layer was deposited using ALD [9]. The polymeric matrix served the purpose of limiting the volume change of the electrode during the Li plating/stripping process. The ZnO was supposed to create a lithiophilic pathway for the Li metal to flow through and infuse in to the polymeric matrix. This is displayed schematically in figure 2.9.

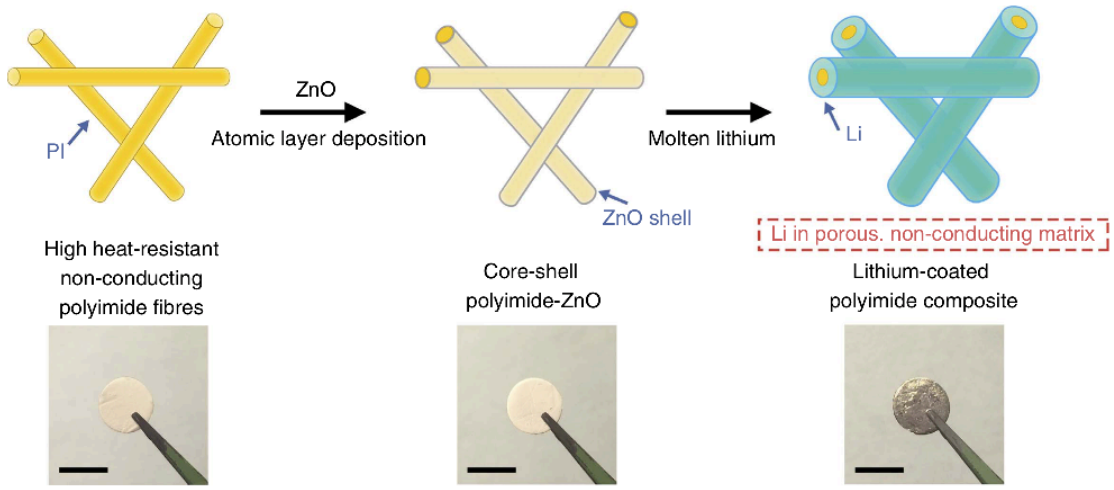

Figure 2.9: A electron polyimide (PI) matrix is coated with ZnO using ALD to render it lithiophillic. Source: [9]

Why does ZnO create a lithiophillic environment? ZnO has been studied as a possible anode material

in Li-ion batteries, instead of graphite. It offers a much higher capacity of $978mAh/g$ (v/s $372mAh/g$ for graphite). However, the capacity fades dramatically with cycling. The following reasons have been proposed to explain this [21]:

1. The reaction of Li with ZnO takes place in 2 steps: (1) oxidation of Li by ZnO to Li_2O and formation of metallic Zn (2) alloying of metallic Li and Zn to form $Li-Zn$ alloys (this alloying is a multi-step process). Step 1 (oxidation of Li to Li_2O) is considered irreversible and contributes significantly to the capacity loss over cycles.

2. Some of the alloys of Li and Zn may be highly crystalline and slow down Li^+ ion transport. The volume changes during alloying may also microstructural changes that affect reversibility.

3. Over multiple cycles metallic Zn crystallises with bulk properties and phase separates. The remaining Li_2O, which is not electrochemically active, acts as an insulating shell that prevents further alloying of Li and Zn [21].

The cycling performance of ZnO thin films v/s Li has been studied previously. The thin films were usually obtained by electrochemical deposition, pulsed laser deposition (PLD) or rf-magnetron sputtering. No literature has thus far been found that studied the electrochemical performance of ZnO thin films deposited by atomic layer deposition (ALD). The studies corroborate the 2-step reaction mechanism described above. It appears that the ZnO structure is modified as the amount of Li reacted increases. This is displayed in figure 2.10 using the discharge curve of a PLD-deposited ZnO thin film v/s Li (ex-situ XRD results in-set).

Note: the peaks attributed to $LiZn$ are only a working assumption, based on the results of XPS measurements.

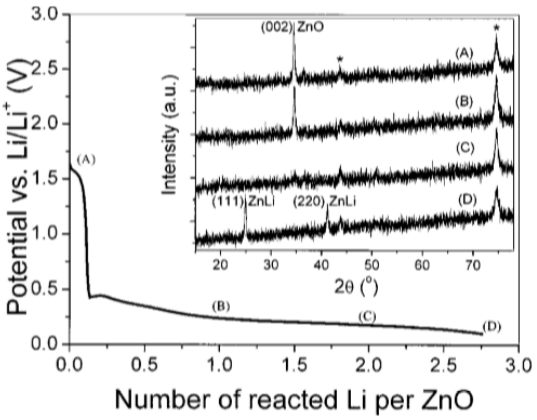

Figure 2.10: Ex-situ XRD pattern of ZnO at varying degrees of discharge v/s Li anode. Source: [10]

It has also been observed that the addition of ZnO quantum dots to a carbon matrix for Li plating/stripping improves the performance of the cell. The formation of highly conductive $LiZn$ alloys provides a favourable path for Li deposition. This reduced the overpotentials required and increases homogeneity of the deposition. The explanation is shown schematically in figure 2.11.

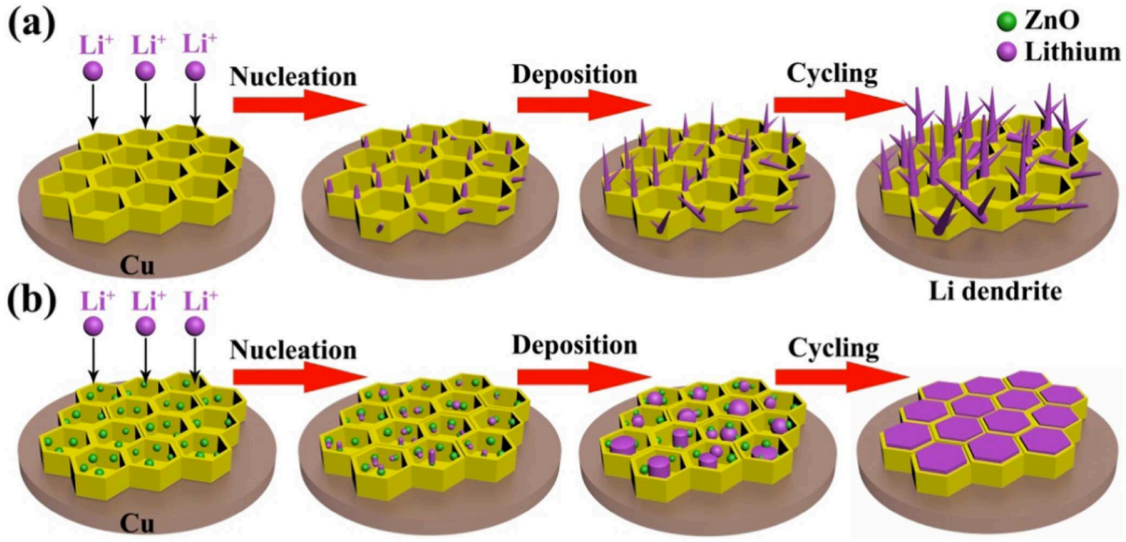

Figure 2.11: Preferential deposition of Li on ZnO nanoparticles

Suppose the reduction of Li by ZnO is controlled in such a way that the alloying reaction between Li and Zn is instead favoured. It is then possible that the plating of Li on a current collector (e.g. copper substrate) through an interfacial ZnO layer is made easier and reversible. The metallic Zn may provide initial nucleation sites upon which the Li can deposit homogeneously. The investigation of such a mechanism is the 2nd aim of this thesis project.

3

Experimental Methods

This chapter chapter will contain a review of the experimental methods that will be used in this thesis. There will be explanations on the scientific principles behind the experiments, and what specific parameters needed to determined to successfully. Some parameters can already be found using literature, while others will be experimentally determined.

3.1. Synthesis of Polymer Electrolyte

The development of the polymer electrolyte took place over a 3 month period at the Holst Centre, TNO. The following parameters were determined for the successful synthesis of the polymer electrolyte:

Figure 3.1: Glove box in which polymer electrolyte synthesis took place

- Type of polymer, salt and solvent
- Ratios of polymer, salt and solvent
- Stirring time and temperature of electrolyte solution

- Type of substrate for casting of thin films
- Wet film thickness of casting (for desired dry film thickness of $100\mu m$)
- Drying conditions for the thin films after casting

3.1.1. Established parameters

Some parameters for the synthesis of the polymer electrolyte determined using literature and did not merit further investigation. The choices were based on desired properties and availability of materials. These are listed in table figure 3.1:

Polymer	Polyethylene oxide (PEO) 600K
Salt	Lithium bis(trifluoromethanesulfonyl)imide ($LiTFSI$)
$EO:Li$	$20:1$
Solution stirring time/temp	$2h/60°C$
Casting method	Blade casting
Film drying time/temp	$12h/R.T.$ (argon) + $12h/60°C$ (vacuum)
Dry film thickness (desired)	$100\mu m$

Table 3.1: Parameters for polymer electrolyte synthesis obtained from literature

The materials and equipment used are presented in figure 3.2. From left to right: heating plate, acetonitrile, polyethylene oxide, lithium bis(trifluoromethanesulfonyl)imide, stirring bars, viol, and weighing scale. At the bottom of the image lie the casting plate and the syringe with needle.

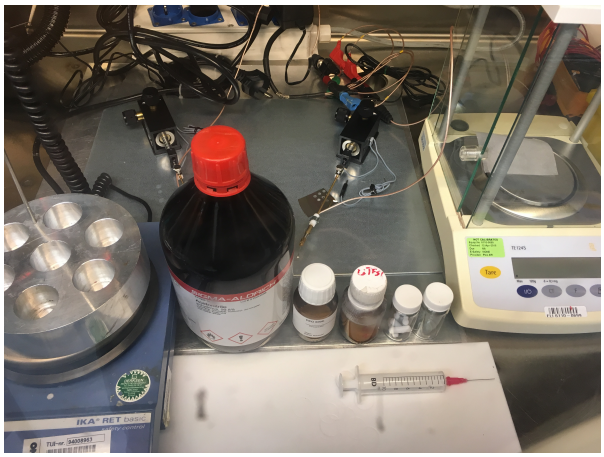

Figure 3.2: Materials and equipment used for electrolyte synthesis

3.1.2. Investigated parameters

Thus, the following needed to be established by experimentation:

1. Solvent concentration
2. Wet film thickness
3. Substrate type optimisation
4. Film drying conditions

3.2. Electro-impedance Spectroscopy (EIS)

Source: [11]

Electrochemical impedance is usually measured by applying an AC potential to an electrochemical cell and then measuring the current through the cell. Assume that we apply a sinusoidal potential excitation. The response to this potential is an AC current signal. This current signal can be analysed as a sum of sinusoidal functions (a Fourier series). A small excitation signal is used so that the cell's response is pseudo-linear. In a linear (or pseudo-linear) system, the current response to a sinusoidal potential will be a sinusoid at the same frequency but shifted in phase. If we plot the applied sinusoidal voltage signal $E(t)$ on the x-axis of a graph and the sinusoidal current response signal $I(t)$ on the y-axis, the result is an oval. This oval is known as a "Lissajous Figure".

If the potential is described as $E_t = E_o exp(jwt)$ and the current response as $I_t = I_o exp(jwt - \phi)$ then the impedance is represented as a complex number as follows:

$$Z(w) = \frac{E(w)}{I(w)} = Z_o exp(\phi) = Z_o(cos\phi + jsin\phi) \tag{3.1}$$

The expression for $Z(\omega)$ is composed of a real and an imaginary part. If the real part is plotted on the X-axis and the imaginary part is plotted on the Y-axis of a chart, we get a "Nyquist Plot" (figure 3.3). In this plot the y-axis is negative and each point on the Nyquist Plot is the impedance at one frequency. Low frequency data are on the right side of the plot and higher frequencies are on the left. This results in the predominance of corresponding processes in the cell.

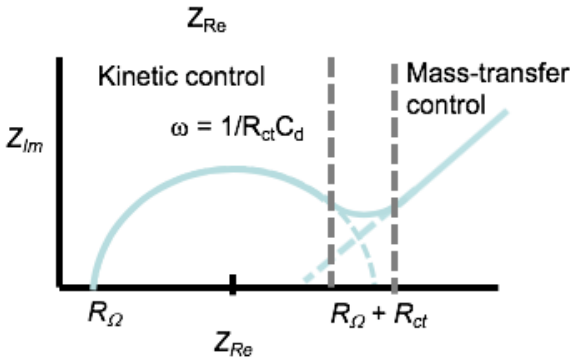

Figure 3.3: Example of a Nyquist Plot. Source: [11]

3.2.1. Equivalent circuit models

A cell, in general, does not contain inductive elements. If they are visible in the EIS results, it is likely to be the result of the connections (wires/plugs) of the test apparatus. The cell will contain capacitive and resistive elements. The impedance of a capacitor is inversely proportional to the frequency ($Z = (jwC)^{-1}$), which means that at higher frequencies capacitors essentially short the other parallel branches of the circuit. A capacitor element in parallel with a resistor gives rise to a characteristic semi-circle in the Nyquist plot. The bulk properties of polymer electrolytes are responsible for the semi-circles seen in their Nyquist plots. The dielectric properties of the film provide the capacitive impedance and the ionic resistance provides the resistive impedance. There also exist circuit elements whose properties are intermediate to a pure capacitor or resistor. These are known are Constant Phase Elements (CPE). The CPE is an circuit element whose impedance is proportional to an exponential power of the frequency. The exponent ranges from 0 (pure resistor) to 1 (pure capacitor).

A special case of CPE is the Warburg impedance which is used to model smooth, porous electrodes. The exponent of proportionality of impedance to frequency is $-1/2$. It can be modelled by an infinite transmission line as shown in figure 3.4.

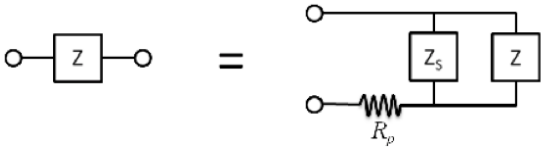

Figure 3.4: Transmission line model which yields the Warburg element on recursion. Source: [12]

Strictly, to obtain the electrolyte resistance from the EIS measurements, the results must be fitted to equivalent circuit models. However, attempting to precisely fit real cells to idealised models is fraught with error. The values that emerge can often be misleading. For the purposes of this report, a mixed quantitative-qualitative assessment of the results will be used.

Among the most commonly used idealised circuit models is the Randles-Esher circuit. The double-layer capacitance of the interface is in parallel with the charge transfer resistance and a Warburg element. The electrolyte resistance is in series with the parallel branches. A mixed kinetic-diffusion controlled process is obtained at low frequencies. The circuit diagram is shown in figure 3.5.

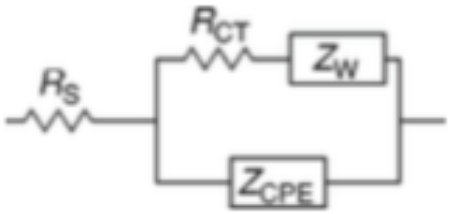

Figure 3.5: Randles circuit diagram. Source: [12]

The Randles-Esher model, however, is better suited to cells with active (non-blocking) electrodes, because the dielectric behaviour of the electrolyte is negligible. Any electric field developed across the electrolyte due to concentration gradients is dissipated by the absorption of ions at the electrodes. For blocking electrodes, an alternative circuit model, sometimes referred to as the Debye circuit, is used. The model is so named because it follows the Debye equations for dielectric relaxation. The electrolyte resistance is in series with the Warburg element and double-layer capacitance. These 3 elements are in parallel with the electrolyte capacitance. The Debye equivalent circuit is displayed in figure 3.6.

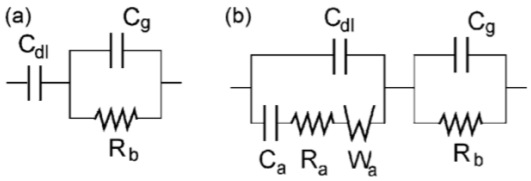

Figure 3.6: Debye circuits with ideal and non-ideal blocking electrodes. Source: [13]

The two models produce slightly different Nyquist plots, which must be accounted for in this report. In the conductivity measurements of the polymer electrolyte, blocking stainless steel (SS) electrodes are used. Thus, the dielectric properties of the electrolyte are enhanced and the Debye model is more suitable. Therefore, the electrolyte resistance can be found from the lower frequency abscissa of the

Nyquist plot.

In the measurement of the transference number, conductive Li electrodes are used. Thus, the Randles-Esher model is more suitable, in which the electrolyte resistance is then represented by the higher frequency abscissa in the Nyquist plot. The low frequency region in the Randles-Esher model represented the processes occurring at the electrode-electrolyte interface.

3.2.2. Transference number

The ratio of the charge carried by an ionic species across a fixed reference plane to the total charge carried by all species across the same plane is called the transference number. For Li ions in a binary solution, the only other current carrying species is the corresponding anion in the Li salt. However, since anion does not engage in reversible reactions at the electrode, a concentration gradient is developed across the cell on the application of an external potential [22]. This concentration gradient further gives rise to an overpotential that must be overcome as long as the cell is operating [14]. Also, at high current densities the power output of the cell is limited by the number of cations available for conduction and reactions. Thus, a high transference is an important target to achieve in polymer electrolytes for commercial applications.

The standard technique to measure the transference number of polymer electrolytes was developed by Bruce et. al [23]. It utilises a symmetric cell with Li electrodes that absorb the Li cation. Once the cell has been polarised, the following processes occur:

1. **Reduction in anionic motion**: Initially, both cationic and anionic conduction take place, which drives the high current across the cell.

2. **Overpotential formation due development of concentration gradients**: However, the anions are not electrochemically active. Thus, they do not get absorbed the anode (unlike the cations at the cathode). This causes an excess concentration of anions near the electrodes. This concentration gradient generates an electric field, inhibiting further anionic motion. This causes a drop in the current across the cell.

3. **Compensatory cationic motion**: To maintain electroneutrality in the face of the anion concentration gradient, compensatory cationic motion from the cathode to the anode occurs. This is in the opposite direction to cationic motion due to the externally applied potential, which is from the anode to the cathode. The balance between these two processes creates a steady-state current value.

The effects of the electrolyte-electrode interface in the polarisation process are also taken into account in this technique. The following equation corrects for the value obtained by simply dividing the steady-state and initial currents:

$$t_{Li^+} = \frac{I_o(\Delta V - I_o R_o)}{I_{ss}(\Delta V - I_{ss} R_{ss})} \tag{3.2}$$

I_o and I_{ss} are the initial and steady state currents, R_o and R_{ss} and the initial and steady state electrode-electrolyte interfacial resistance, and ΔV is the applied potential. The resistances are read from the corresponding Nyquist plots, and the currents from the chronoamperometry plot (current v/s time). The first Nyquist measurements are taken before the external voltage is applied and the second are taken once the current has reached its steady state value. The types of plots expected are shown in figures 3.7 and 3.8:

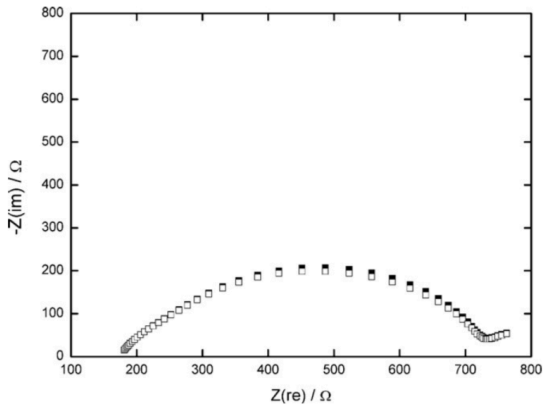

Figure 3.7: Sample Nyquist plot for transference number with equivalent circuit in-set. Source: [14]

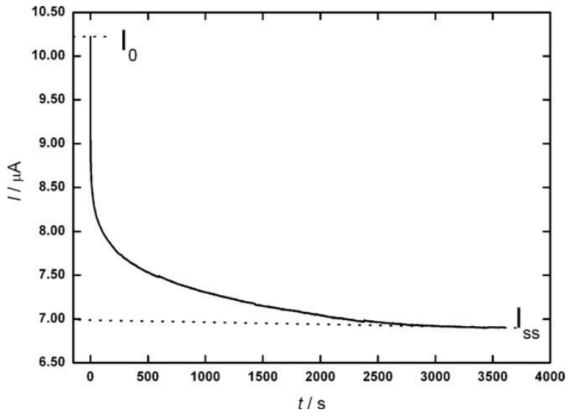

Figure 3.8: Sample chronoamperometry plot for transference number. Source: [14]

3.3. Atomic Layer Deposition (ALD)

Source: [15]

ALD is a particular case of chemical vapour deposition (CVD). In conventional ALD, precursors are injected time-sequentially in the deposition zone, reacting one at a time with active sites on the substrate surface through selective and self-limiting half-reactions, each one being separated by purge steps to remove all unreacted precursor and reaction products in the gas phase. In CVD, on the other hand, reactions take place above the substrate. The nature of ALD precursors allows the deposition of high-quality materials at lower temperatures than with CVD, even near room temperature.

3.3.1. spatial-ALD

ALD can be defined by its particular temperature dependence. The growth takes place only in a characteristic temperature window, since at low temperatures, precursor molecules cannot be sufficiently activated, or desorption can be too slow. At high temperatures, precursors can decompose at the surface or even before reaching it, and desorption can be too fast during the purge step. The entire process mostly takes place at elevated temperatures (thermal ALD) and at low reactor pressure or with a plasma source coupled (plasma enhanced ALD) to improve the deposition. However, this is dependent on the nature of the precursors and the substrate since depositions are possible even at temperatures even below $100°C$. The process is shown schematically in figure 3.9. The sections of the schematic are: 3.9 (a) reactor cross-section 3.9 (b) reactor bottom 3.9 (c) reactor

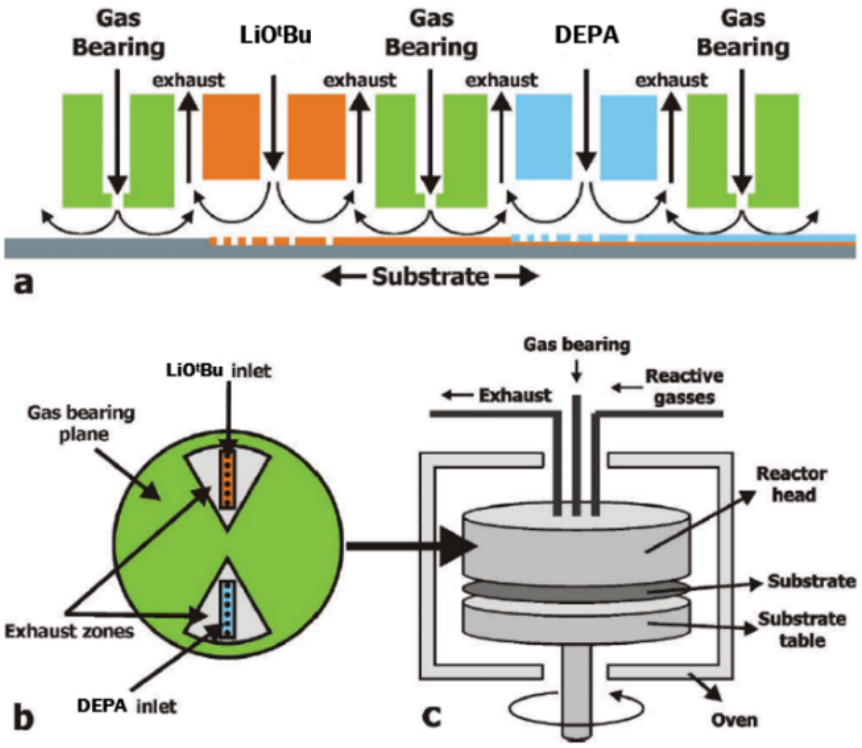

Figure 3.9: Schematic diagrams for the spatial-ALD. Source: [15]

The purging of the reactor is a time consuming step which severely limits the deposition speed of conventional ALD. This drawback has been overcome by the spatial atomic layer deposition (sALD) technique. In s-ALD the dosage of the precursors occurs in different space-divided zones of the reactor and a moving substrate is sequentially exposed to each of these zones, as shown in figure 3.9. By spatially dividing them by a nitrogen gas curtain, a purge step is no longer needed and deposition rates can be up to two orders of magnitude faster (from $0.01nm/s$ to $1.0nm/s$). Additionally, sALD can be

easily performed at ambient atmosphere, making it is easier and cheaper to scale up than conventional ALD. This opens the door to widespread industrial application in high-quality films fully suited for device integration in fields within solar energy, energy storage, or smart windows.

3.3.2. Deposition of ZnO

For ZnO, diethylzinc [$Zn(C_2H_5)_2$, or DEZ] and water (H_2O) have been used as zinc and oxygen precursors, respectively. Precursors are evaporated from bubblers, by using argon as a carrier gas, and transported to the reactor head through heated lines, to prevent condensation. Growth per cycle of $0.18nm/cycle$ (see figure 3.10) at rotation frequency of $5Hz$ results in a deposition rate of $0.9nm/s$, which is about hundred of times faster than the deposition rate typically achieved by conventional ALD ($\sim 0.01nm/s$) and comparable to the growth rate achieved by industrially scalable deposition techniques, as PE-CVD and sputtering.

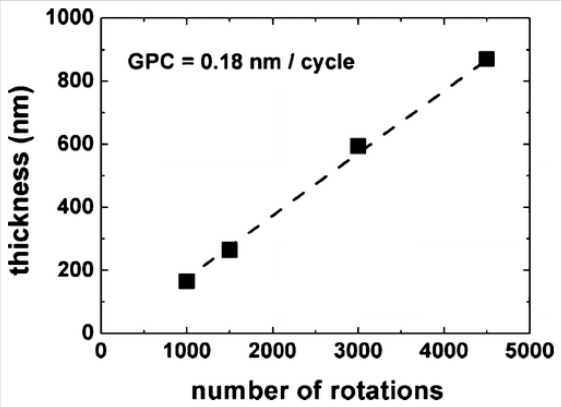

Figure 3.10: Growth per cycle (GPC) of ZnO in s-ALD. Source: [15]

In this thesis, the depositions took place the s-ALD reactor at Solliance, under the aegis of the Holst Centre. We used 900 cycles of deposition at a rotation frequency of $100rpm$ ($= 1.67Hz$). The depositions took place at $200°C$ and the target thickness of the ZnO film was around $150nm$. The substrate for the deposition were copper foils of $10\mu m$ thickness obtained from TU Delft. A picture of the deposited substrate is shown in figure 3.11.

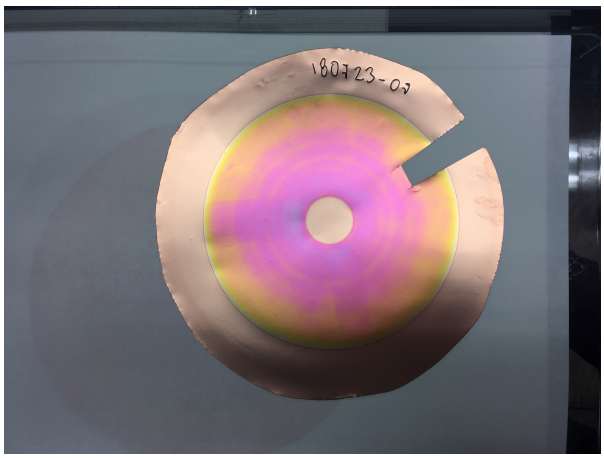

Figure 3.11: ZnO layer deposited by s-ALD on a copper substrate

3.4. Scanning Electron Microscopy (SEM)

Source: [24], [25], [26]

The scanning electron microscope (SEM) uses a focused beam of high-energy electrons to generate a variety of signals at the surface of solid specimens. The signals that derive from electron-sample interactions reveal information about the sample including external morphology (texture), chemical composition, and crystalline structure and orientation of materials making up the sample. In most applications, data are collected over a selected area of the surface of the sample, and a 2-dimensional image is generated that displays spatial variations in these properties. Areas ranging from approximately $1cm$ to $5\mu m$ in width can be imaged in a scanning mode using conventional SEM techniques.

The SEM is also capable of performing analyses of selected point locations on the sample; this approach is especially useful in qualitatively or semi-quantitatively determining chemical compositions (using EDS/EDX), crystalline structure, and crystal orientations (using EBSD). The design and function of the SEM is very similar to the EPMA and considerable overlap in capabilities exists between the two instruments. SEM analysis is considered to be ”non-destructive”; that is, X-rays generated by electron interactions do not lead to volume loss of the sample, so it is possible to analyze the same materials repeatedly. An example of an EDX plot used for elemental characterisation is shown in 3.12.

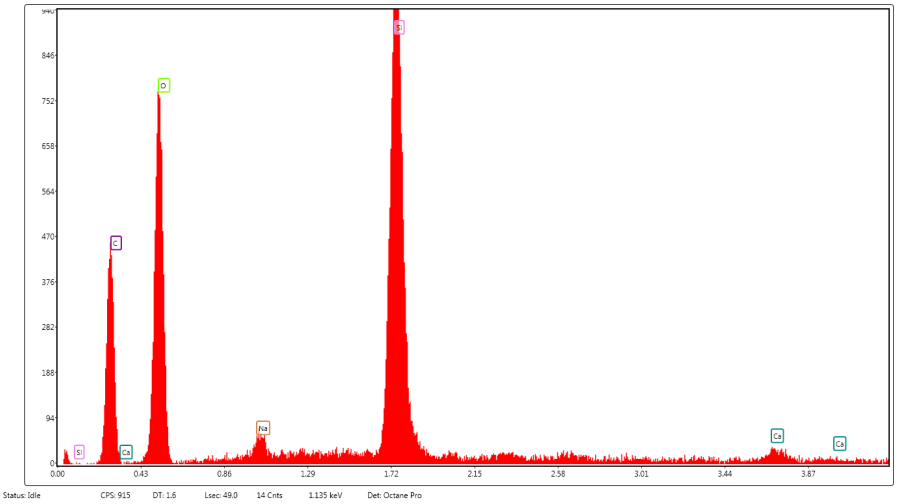

Figure 3.12: Example of an EDX spectrum

3.4.1. Interactions between electrons and sample

Accelerated electrons in an SEM carry significant amounts of kinetic energy, and this energy is dissipated as a variety of signals produced by electron-sample interactions when the incident electrons are decelerated in the solid sample. These signals include secondary electrons (that produce SEM images), backscattered electrons (BSE), diffracted backscattered electrons (EBSD that are used to determine crystal structures and orientations of minerals), photons (characteristic X-rays that are used for elemental analysis and continuum X-rays), visible light (cathodoluminescence–CL), and heat. Secondary electrons and backscattered electrons are commonly used for imaging samples: secondary electrons are most valuable for showing morphology and topography on samples and backscattered electrons are most valuable for illustrating contrasts in composition in multiphase samples (i.e. for rapid phase discrimination).

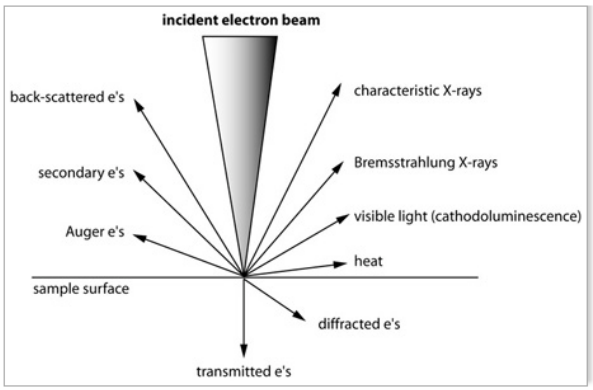

Figure 3.13: Types of interactions between the electron and the sample

3.4.2. Interactions within a sample

X-ray generation is produced by inelastic collisions of the incident electrons with electrons in discrete orbitals (shells) of atoms in the sample. As the excited electrons return to lower energy states, they yield X-rays that are of a fixed wavelength (that is related to the difference in energy levels of electrons in different shells for a given element). Thus, characteristic X-rays are produced for each element in a mineral that is "excited" by the electron beam. Where an electron beam impinges on a sample, electron scattering and photon- and X-ray-production develops in a volume (the electron interaction volume) that is dependent on several factors. These include:

1. The energy of the incident beam (accelerating potential) increases the interaction volume, but decreases the elastic scattering (e.g. backscattering).
2. The interaction volume decreases as a function of the mean atomic weight.
3. Smaller and more asymmetric interaction volumes develop in samples tilted relative to the impinging electron beam.

Each of the signals used for imaging or X-ray generation is generated from different electron interaction volumes and, in turn, each of the signals has different imaging or analytical resolution. Auger and Secondary images have the best imaging resolution, being generated in the smallest volume near the surface of the sample. Backscattered electrons are generated over a larger volume resulting in images of intermediate resolution. Cathodoluminescence is generated over the largest volume, even larger than Bremsstrahlung radiation, resulting in images with the poorest resolution.

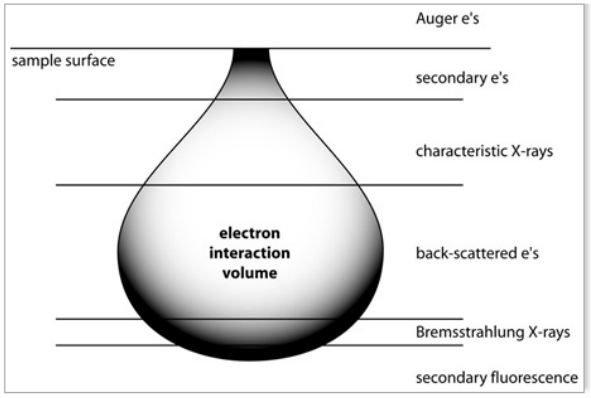

Figure 3.14: Interaction of electron within the sample volume

3.5. X-Ray Diffraction (XRD)

Source: [27], [28]

X-ray diffraction (XRD) is a rapid analytical technique primarily used for phase identification of a crystalline material and can provide information on unit cell dimensions. X-ray diffraction is based on constructive interference of monochromatic X-rays and a crystalline sample. These X-rays are generated by a cathode ray tube, filtered to produce monochromatic radiation, collimated to concentrate, and directed toward the sample. The interaction of the incident rays with the sample produces constructive interference (and a diffracted ray) when conditions satisfy Bragg's Law ($n\lambda = 2dsin\theta$).

When a crystal is bombarded with X-rays of a fixed wavelength (similar to spacing of the atomic-scale crystal lattice planes) and at certain incident angles, intense reflected X-rays are produced when the wavelengths of the scattered X-rays interfere constructively. In order for the waves to interfere constructively, the differences in the travel path must be equal to integer multiples of the wavelength. When this constructive interference occurs, a diffracted beam of X-rays will leave the crystal at an angle equal to that of the incident beam.

3.5.1. Bragg's Law

Bragg's law relates the wavelength of electromagnetic radiation to the diffraction angle and the lattice spacing in a crystalline sample. These diffracted X-rays are then detected, processed and counted. By scanning the sample through a range of 2θ angles, all possible diffraction directions of the lattice should be attained due to the random orientation of the powdered material. Conversion of the diffraction peaks to d-spacings allows identification of the mineral because each mineral has a set of unique d-spacings. Typically, this is achieved by comparison of d-spacings with standard reference patterns.

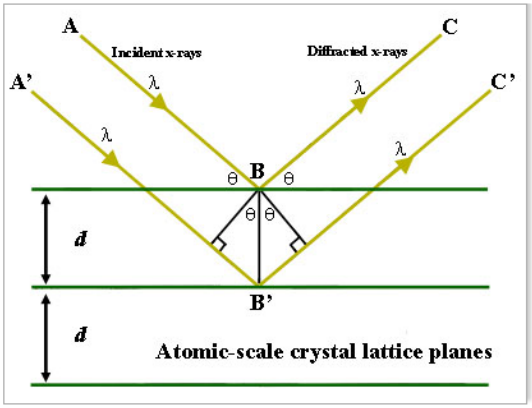

Figure 3.15: Principle of operation of XRD - constructive interference of reflected rays

All diffraction methods are based on generation of X-rays in an X-ray tube. These X-rays are directed at the sample, and the diffracted rays are collected. A key component of all diffraction is the angle between the incident and diffracted rays. Powder and single crystal diffraction vary in instrumentation beyond this.

3.5.2. X-ray diffractometer

X-ray diffractometers consist of three basic elements: an X-ray tube, a sample holder, and an X-ray detector. X-rays are generated in a cathode ray tube by heating a filament to produce electrons, accelerating the electrons toward a target by applying a voltage, and bombarding the target material with electrons. When electrons have sufficient energy to dislodge inner shell electrons of the target material, characteristic X-ray spectra are produced.

These spectra consist of several components, the most common being Kα and $K\beta$. $K\alpha$ consists, in

part, of $K\alpha 1$ and $K\alpha 2$. $K\alpha 1$ has a slightly shorter wavelength and twice the intensity as $K\alpha 2$. The specific wavelengths are characteristic of the target material (Cu, Fe, Mo, Cr). Filtering, by foils or crystal monochrometers, is required to produce monochromatic X-rays needed for diffraction. $K\alpha 1$ and $K\alpha 2$ are sufficiently close in wavelength such that a weighted average of the two is used.

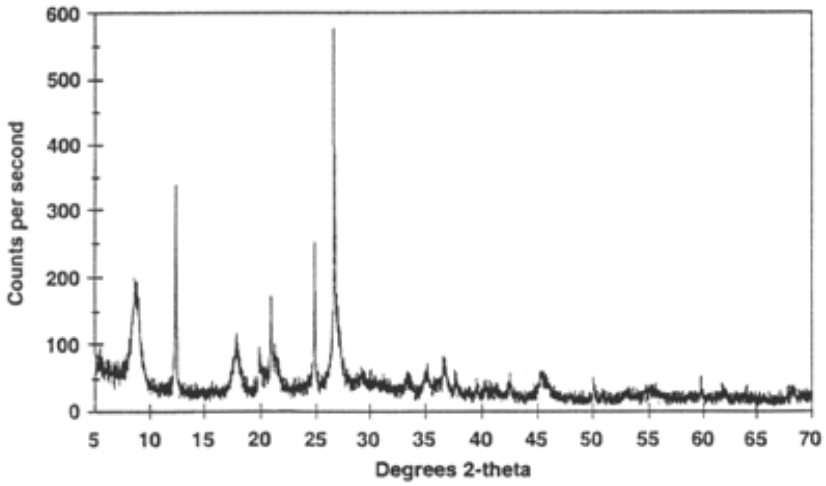

Figure 3.16: Example of a XRD diffractogram

Copper is the most common target material for single-crystal diffraction, with $CuK\alpha$ radiation = 1.5418. These X-rays are collimated and directed onto the sample. As the sample and detector are rotated, the intensity of the reflected X-rays is recorded. When the geometry of the incident X-rays impinging the sample satisfies the Bragg Equation, constructive interference occurs and a peak in intensity occurs. A detector records and processes this X-ray signal and converts the signal to a count rate which is then output to a device such as a printer or computer monitor.

The geometry of an X-ray diffractometer is such that the sample rotates in the path of the collimated X-ray beam at an angle θ while the X-ray detector is mounted on an arm to collect the diffracted X-rays and rotates at an angle of 2θ. The instrument used to maintain the angle and rotate the sample is termed a goniometer. For typical powder patterns, data is collected at 2θ from $5°$ to $70°$, angles that are preset in the X-ray scan.

3.6. Li Plating/Stripping

Li is a conversion-pattern host-less anode, not an insertion host. Li ions from the electrolyte get reduced and deposit on Li metal. Since it is not a host, the capacity of a Li metal anode is technically infinite. The capacity is instead calculated in terms of the theoretical charge capacity of Li.

$$Q_c = \frac{charge}{mass} = \frac{6.02x10^{23} atoms (1.6x10^{-19} C/atom) \frac{1mAh}{3.6C}}{6.94 g/mol} = 3.86x10^3 mAh/g \quad (3.3)$$

The stripping/plating of Li is performed in much the same way as a cell is cycled. The key difference here is, unlike in cycling tests, the cells must be forced to discharge to negative potentials. This means that the cell is being forced to push Li across the electrolyte even after the cell is not naturally inclined to do so. The Li is then stripped to a cut-off voltage in the charging process. The cut-off is required since the voltage tends to spike when the last bits of Li are being stripped.

In order to ensure consistency of results with fewer variables, the predicted amount of Li that is plated was fixed at $0.5 mAh/cm^2$. In reality, the amount of Li plated was lower since some of it is also consumed in parasitic side-reactions. The current densities in the cell were varied from $0.1 mA/cm^2$ to $10 mA/cm^2$. The cells did not show appreciable difference in performance at very low current densities, but this was because each cycle took much longer to perform. Therefore, only a limited comparison could be made at these currents. Thus, the results are presented for 1, 5 and $10 mA/cm^2$. The cells used for the tests consisted of:

1. Stainless steel (SS) disc
2. Li foil
3. Whatman separator
4. 50 µl of 1 M $LiPF_6$ in EC/DMC
5. Copper foil/ZnO on copper foil
6. SS disc
7. Spring

The setup used to assemble the cells is shown in figure 3.17.

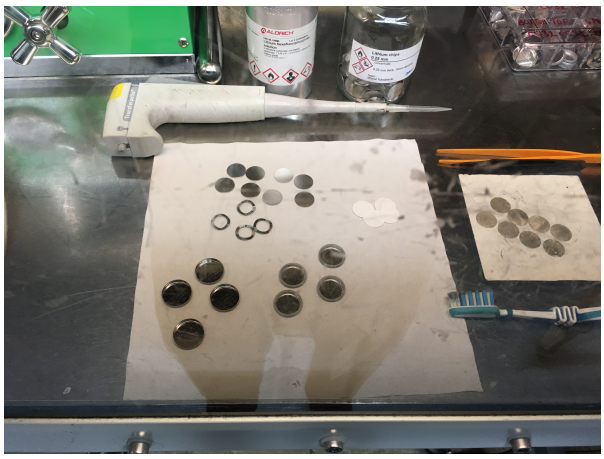

Figure 3.17: Set up for the assembly of cells used in the Li plating/stripping experiments

4

Results & Discussions

This chapter contains a detailed discussion of the major results from the thesis project. The aim is to show how the results were arrived at, what conclusions can be drawn from them and how these conclusions led to further investigations. Some additional results which were worth investigating but ultimately did not assist in forming conclusions during the course of this project are discussed briefly in the Appendices.

4.1. Synthesis of Polymer Electrolyte

The synthesis of the polymer electrolyte was by some distance the most challenging task of the thesis. More than 50 samples were made before a reproducible method of synthesis with the desired properties was obtained. In total, more than 100 samples were made to conduct all required characterisation experiments. The films were extremely difficult to handle and sensitive to each step of the preparation process. In particular, the presence of powder contaminants or minor disturbances in the drying process needed to be critically controlled. A picture of one of the films in shown in figure 4.1.

Figure 4.1: The polymer film obtained after all optimisation processes

4.1.1. Experimentally determined parameters

The first parameter that was optimised was the concentration of the solvent, acetonitrile (ACN). The weight percentages ranged from 25% to 95%. The 2 properties that needed to be monitored were homogeneity and viscosity. The homogeneity is required to ensure uniform distribution of the chemicals in the electrolyte. The viscosity is required to regulate the flow of the wet film after casting. Eventually, 90% was chosen as the ideal solvent concentration.

Solvent % (wt./wt.)	Properties
25%	Incomplete dissolution of the solute components.
50%	Solute components dissolved well. But, the solution had very high viscosity. It did not flow easily when casting was attempted.
75%	Similar dissolution of solute components to 50%. Again, solution had very high viscosity. Properties were superior to 50% sample.
90%	Excellent dissolution of solute components Viscosity of the solution was ideal. Mixture flowed well on casting substrate.
95%	Solute components dissolved but viscosity was too low. Flow was not easily contained on casting substrate. 90% had more suitable properties

Table 4.1: Solvent % optimisation process

The next step was to optimise the casting substrate. The key requirements were a smooth surface and chemical inertness against the components of the solution. It was also important that the substrate did not adhere strongly to the film for the lifting process. While glass is a commonly used substrate material, we found that polymer films adhered strongly to the surface and the films tore while attempting to lift them from the substrate. Polyethylene was also attempted simply because the material was available, but it did not give any better results. Finally, Teflon (PTFE) plates were used. The non-stick property of the material meant that the films lifted off easily after drying. Later in the project, stainless steel (SS) plates with a Teflon layer on top were used.

Casting substrate material	Properties
Glass	Film stuck strongly to the substrate
Polyethylene	Film again stuck strongly to the substrate
Teflon	Film could be lifted off with ease

Table 4.2: Choice of casting substrate

The project aimed to have a dry-film thickness of around $100\mu m$. The wet film thickness needed to higher by several factors, since 90% of the film comprised of the solvent. A range of values from $1000 - 1500\mu m$ were attempted. $1500\mu m$ was the upper limit of the blade casting device used to cast the films. The dry-film thickness varied across the dimensions of the films, since the solution did not flow evenly. A wet-film thickness of about $1500\mu m$ ensured that most of the film had a dry thickness of $90 - 110\mu m$, which met the requirements.

Wet film thickness (μm)	Properties
1000	Dry film was too thin and tore apart easily
1200	Dry film did not tear apart but thickness was $60 - 80\mu m$
1500	Dry film lifted easily with a thickness of $80 - 100\mu m$

Table 4.3: Optimisation of wet-film casting thickness

At the end of these optimisation attempts, we finally achieved the goal of a thin, solvent-free polymer

membrane. It was still difficult to cut discs required for testing in cells as the films did not cut easily and were sometimes still prone to tearing. This may be due to the remnants of moisture and solvent that degraded the mechanical strength of the film. As a final step of optimisation, the films were dried for 24 hours under argon at room temperature (instead of 12 hours), and subsequently for 48 hours under vacuum at 60 °C (instead of 12 hours again). We then managed to obtain free-standing films from which a number of samples could be cut on a consistent basis.

4.2. Characterisation of Polymer Electrolyte

The conductivity of the polymer electrolyte was determined using Electroimpedance Spectroscopy (EIS). All experiments were performed in EL-cells with the polymer electrolyte between stainless steel (SS) blocking electrodes. Initially, the frequency range was between $10Hz$ and $0.1MHz$. The upper limit was adjusted to 1 MHz after some initial experiments to catch missing details in high temperature measurements. The DC polarisation voltage was $10mV$ and the amplitude of the AC disturbance was also $10mV$. The cells were pre-heated to $60°C$ to so that the polymer would partially melt and improve the interfacial contact. The cells were allowed to equilibriate for 2 hours for each temperature measurement.

4.2.1. Nyquist plots

Measured Nyquist plots for the polymer electrolyte for temperatures from $25°C$ to $60°C$ is displayed in figure 4.2.

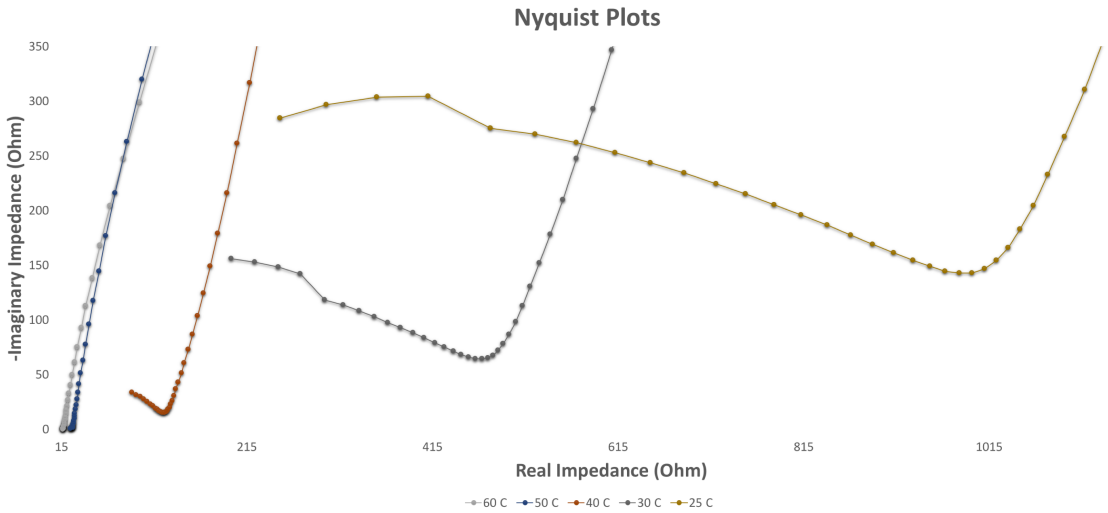

Figure 4.2: Temperature dependent Nyquist plots of the polymer electrolyte

The following characteristics can be easily distinguished:

1. **The semi-circle is only partial and its size increases as the temperature decreases**
   - The semi-circle is partial simply because the upper frequency limit of the measurement was not high enough.
   - The increase in size occurs in both the imaginary and real axes
   - This implies that both the capacitive and resistive elements increase in magnitude
   - Since the resistive element corresponds to the ionic resistance, the decrease with temperature can be due to either: (1) increased ionic mobility (2) increased segmental motion
   - Since the capacitive element corresponds to the dielectric properties of the cell, the change in capacitance can only be due to the change in dielectric constant of the cell

2. **The partial semi-circle intersects with a diagonal line at low frequencies**
    - The behaviour of the system at such frequencies is this not dependent of the bulk properties of the electrolyte but instead on the electrode/electrolyte interface
    - If the line had a slope of $45°$, a Warburg element could have been used to model the processes; their presence signifies a semi-infinite diffusion controlled process
    - Since the slope is not $45°$, a mixed kinetic/diffusion controlled process occurs at the blocking electrodes.
    - The mixed process can instead by modelled using a constant phase element (CPE)
3. **The slope of the diagonal line remains approximately the same across temperatures**
    - This implies the processes occurring at the blocking electrodes are temperature independent
    - Since the electrodes are blocking, the charge-transfer resistance should remain very high regardless of temperature
    - The blocking leads to the formation of a double layer capacitance at the electrode/electrolyte interface
    - This capacitance depends on the concentration of ions in the electrolyte
    - For dilute electrolytes, the diffusive length of the double-layer (Debye length - L_D) is much larger than the size of the ion
    - The limit of dilution is reported to be an $EO : Li$ molar ratio of $10 : 1$ i.e.,the process is kinetically controlled above this concentration
    - Since a lower concentration is used here ($EO : Li = 20 : 1$), the Debye length approaches the size of the ion and pure kinetic control is not feasible
    - This is why the process has a mixed kinetic-diffusion control

4.2.2. Arrhenius plots

As explained in the previous chapter, the lower frequency abscissae of the Nyquist plot are used to obtain the electrolyte resistance. In the measured graphs an abscissa is often not actually obtained due to non-ideality in the measurements. The standard approach in such a scenario is to use the point of the intersection between the extrapolated diagonal line and partial semi-circle. The conductivities were measured from $25°C$ to $60°C$ (except for 2 cells where measurements were taken at $20°C$ instead of $25°C$). The log of the conductivity values (in S/cm) on the y axis are plotted against the reciprocal of the temperature (in $Kelvin$) multiplied by 1000 on the x axis. Such plot are called Arrhenius plot. The results for the all cells successfully tested are shown in figure 4.3.

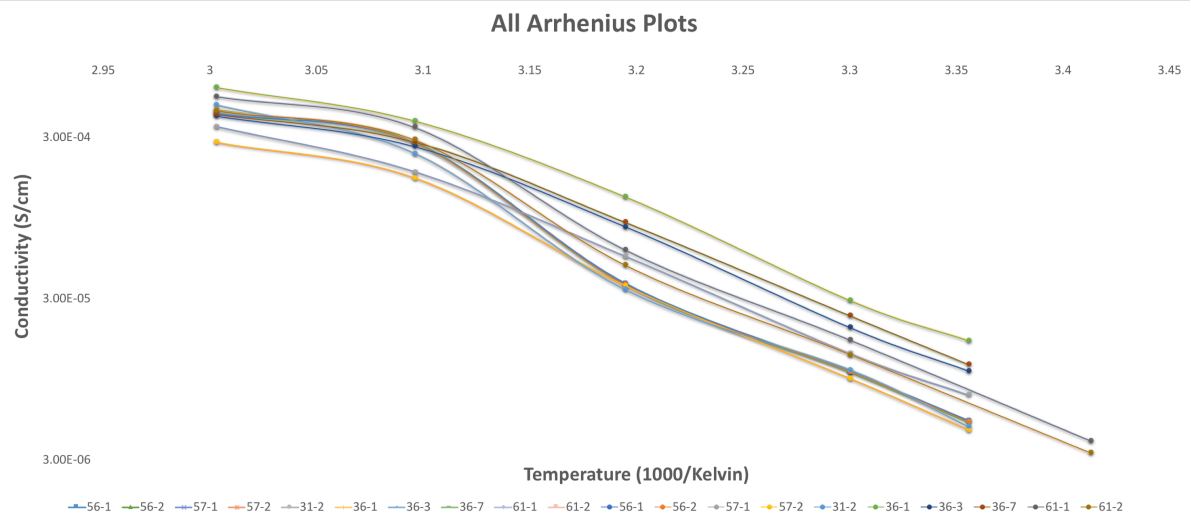

Figure 4.3: Arrhenius Plots of conductivity v/s temperature

The following features are noticeable:

1. **The plots are not linear - they do not follow the Arrhenius conduction model**

   - A linear relationship is expected from the Arrhenius model of the chemical bond breaking and forming $\sigma = Ae^{\frac{-E_a}{k_B T}}$
   - The model specifies A fraction of the molecules have an energy >= the activation energy E_a
   - These molecules exchange energy amongst each other through collisions
   - When the collision energy is greater than the activation energy, reactions occur
   - A temperature independence of the activation energy is assumed
   - This law is often violated in materials that undergo a glass transition (this occurs at around $-70^{\circ}C$ for PEO [29]

2. **The conductivity drops sharply in some samples below** $50^{\circ}C$

   - The non-linearity appears to be largely the result of this sharp change
   - The average activation energy rises sharply from $0.18eV$ to $0.49eV$ and remains similar thereafter (see table 4.4)
   - This suggests that that the mechanism of conduction changes below $50^{\circ}C$

Temperature Range	Activation Energy (eV)
$60^{\circ}C - 50^{\circ}C$	0.18
$50^{\circ}C - 40^{\circ}C$	0.49
$40^{\circ}C - 30^{\circ}C$	0.46
$30^{\circ}C - 25^{\circ}C$	0.45

Table 4.4: Activation energies according to temperature range

After controlling for other possible factors, it was decided to investigate the effect of pressure on the cells. The pressure was varied by changing the thickness of the stack in cells using stainless steel (SS) discs. The working hypothesis was that if the pressure in the cells was higher, the bulk conductivity of the electrolyte should not be affected since it is a solid and not a gas (and thereby incompressible). If there are any variations in measurements, it could be due to the improvement contact between the layers of the cell. Thus, if a consistent trend of pressure dependence was visible, it was possible that the chosen abscissae did not only represent the electrolyte resistance, as was previously assumed.

The pressure was varied between $225kPa$ and $280kPa$ (corresponding to a force of about $45N$ - $55N$ on the cell). The resulting Arrehnius plots are shown in figure 4.4

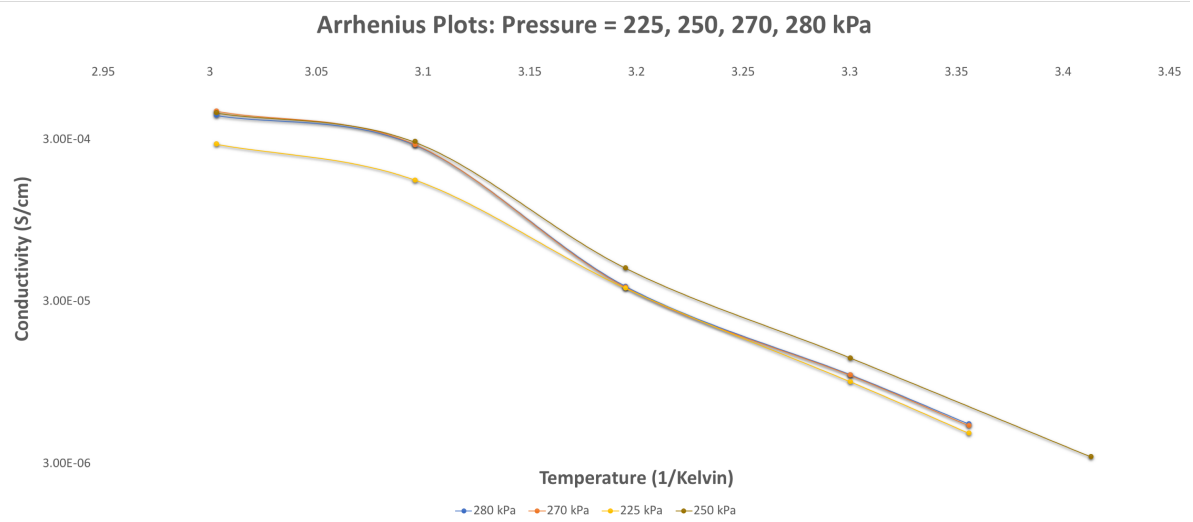

Figure 4.4: Variation of conductivity with temperature for 4 different cell pressures

The following can be observed and inferred:

1. **No appreciable correlation can be found between pressure and conductivity**

   - At $60^{\circ}C$, the sample with the lower pressure does have the lower conductivity
   - But, all other samples have similar values
   - As the temperature drops, the differences in conductivity grow smaller
   - It does appear as though the cells with higher pressure have a sharper drop in conductivity at $50^{\circ}C$

2. **It is clearer that the trend is approximately linear below** $50^{\circ}C$

   - The measurement at $20^{\circ}C$ helps to see this trend
   - This suggests that the behaviour does follow the Arrhenius model in this temperature range - ionic hopping
   - Perhaps the segmental motion of the polymer becomes limited below a certain temperature
   - This is likely to be due to re-crystallisation of the polymer

To verify the effects of pressure, measurements were conducted at constant cell pressure. This should eliminate differences in interfacial contact, if any could arise. An intermediate pressure of $240kPa$ was chosen. The results for are shown in figure 4.5.

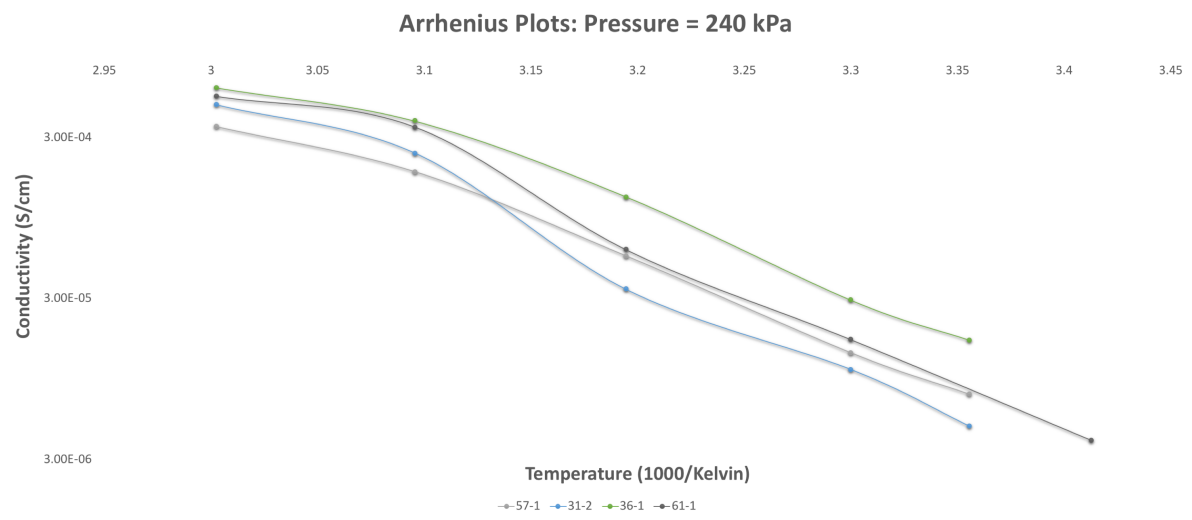

Figure 4.5: Variation of conductivity with temperature at fixed cell pressure

Again, the following can be observed and inferred:

1. **There are still significant differences in conductivity across cells**
   - The values are in fact less similar to each other than the measurements taken at different pressures
   - Slight non-linearity is seen even below $50°C$ for some cells
2. **Two cells show a sharper drop in conductivity after** $50°C$
   - This relative sharpness was previously attributed to higher pressures in some cells
   - This hypothesis can be dropped. Some other factor must be at play

On investigation of the data, it was found the cells that displayed the sharper drops in conductivity after $50°C$ had the measurements taken together. Since all cells had their measurements taken after 2 hours at each temperature, the effect of time at a particular temperature was not likely to be significant. One other possible explanation remains: the cells were placed in an oven with samples for other experiments and projects. If the door to the oven was opened and closed more times in some experiments than the other, there could have been larger disruptions in the equilibriation process. But, the sharp differences are only visible in the $40°C$ - $50°C$ range. This suggests that the sample is more sensitive to the equilibriation process in this temperature range. This is also where decreased segmental motion due to re-crystallisation of the polymer was hypothesised to be taking place.

Thus, a mixed-model of conduction is required that takes into account both Arrhenius modelled ionic-hopping and the segmental motion of the polymer. The model most commonly used in literature is called the Vogel-Tamman-Fulcher (VTF) model [30]. It results in a modified version of the Arrhenius equation:

$$\sigma = AT^{\frac{-1}{2}} exp(\frac{-B}{T - T_o}) \tag{4.1}$$

A is the pre-exponential constant (proportional to the number of carrier ions), B is the pseudo-activation energy for conduction, and T_o is the ideal glass transition temperature. This model uses the notion of a coupling that exists between the conduction of ions and the segmental motion of the polymer. They do not occur as independent process but are instead dependent on the thermal state of the polymer. As the extent of crystallisation increases with the decrease the temperature, the segmental and ionic motions tend to get de-coupled. This results in the expected Arrhenius type behaviour for ionic conduction.

4.2.3. Transference number

The transference number was determined using the potentiostatic polarisation method discussed in the previous chapter. The Nyquist plots before and after polarisation are shown in figure 4.6.

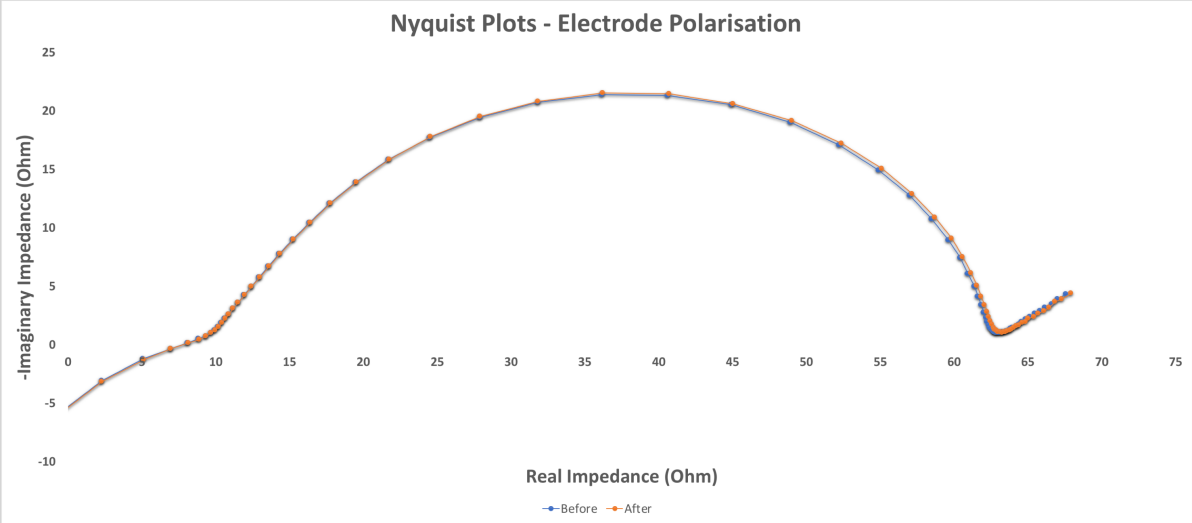

Figure 4.6: Nyquist plots before and after electrode polarisation.

The following characteristics are visible:

1. **The Randles-Esher model is better suited to these plots**

   - We can see a full semi-circle correspond to the behaviour of the electrode-electrolyte interface
   - The higher frequency abscissa corresponding to electrolyte resistance agrees well with the value of the lower frequency abscissa in the plot of blocking electrodes

2. **The interface resistances do not appear to have polarised significantly**

   - In fact, the plot before and after polarisation are almost coincident
   - This suggests that the passivation layers do not generate large overpotentials during cell operation
   - This is an indication of good, stable contact

The current decay is shown in figure 4.7.

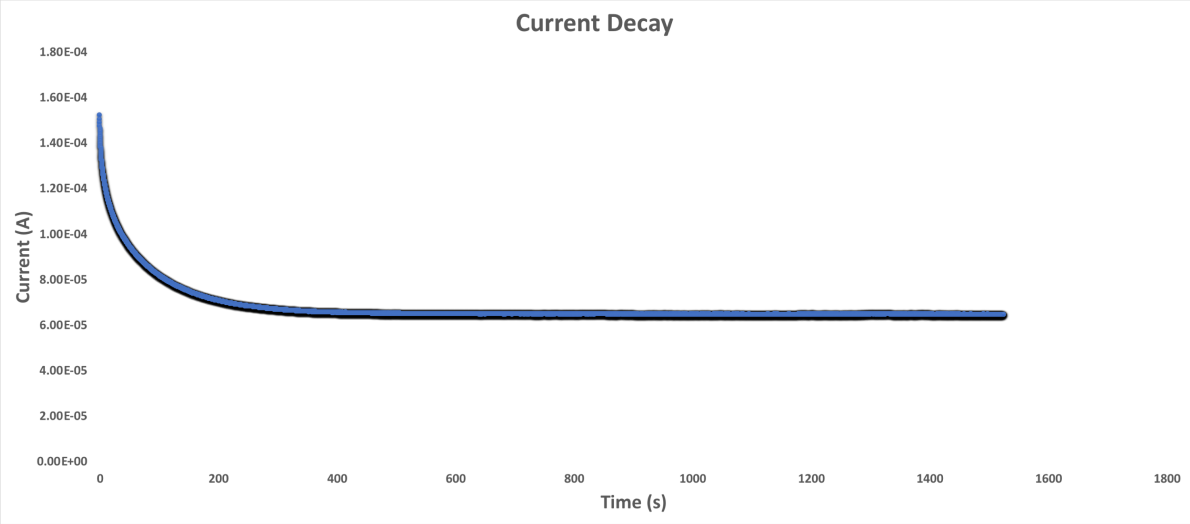

Figure 4.7: Current decay as the concentration gradients are formed.

The requisite parameters from the above charts are listed in table 4.5.

ΔV	$10mV$
I_o	$0.7x10^{-4}A$
R_o	63Ω
I_{ss}	$1.5x10^{-4}A$
R_{ss}	63.5Ω

Table 4.5: Parameters taken from the charts for transference number determination

The transference number is calculated as follows:

$$t_+ = \frac{I_o(\Delta V - I_o R_o)}{I_{ss}(\Delta V - I_{ss}R_{ss})} = \frac{0.7x10^{-4}(0.01 - 0.7x10^{-4}x63)}{1.5x10^{-4}(0.01 - 1.5x10^{-4}x63.5)} = 0.21 \quad (4.2)$$

This value is in accordance with what has been reported in literature [23]. The transference number for polymer electrolytes has been found to have weak dependence on temperature [31]. The dependence is, in fact, strong for the concentration of the salt and the type of anion. But these variations were not attempted in this project.

4.2.4. Addition of Succinonitrile

The development of the polymer electrolyte had by this time progressed further at TU Delft. Dr. Ming Liu at the RID successfully added the plasticiser succinonitrile to the polymer which improved its conductivity at room temperature. While conducting Li plating/stripping tests on the electrolyte, it was found the presence of an interfacial layer of ZnO improved the performance. Thus, the remainder of the thesis was devoted to the investigation of the effects of the interfacial ZnO layer.

4.3. Characterisation of ZnO films

The ZnO films deposited by ALD were characterised using SEM-EDX (XRD was also used unsuccessfully - see Appendix B). The SEM provides a picture of the surface morphology and allows us to estimate the thickness and roughness of the layer. EDX measurements were carried out to examine the elemental composition of the layer.

The SEM results are shown below. In figure 4.8, we get an overview of the surface morphology of the

deposition.

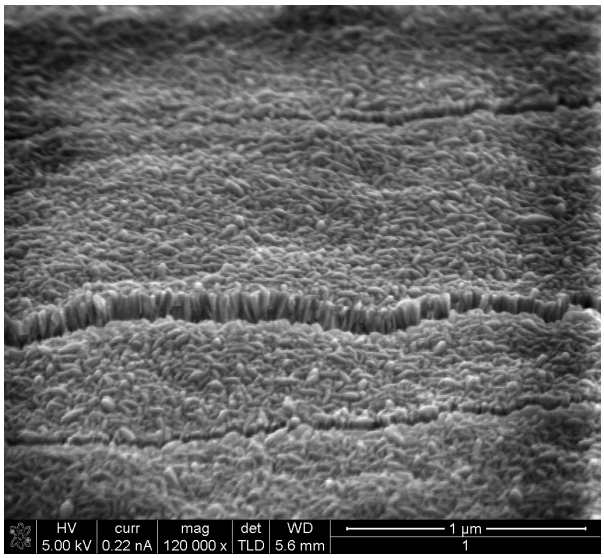

Figure 4.8: Overview of the surface morphology

We see that the layer of ZnO has been deposited uniformly and has the appearance of a regular crystalline structure. There is a significant degree of surface roughness which is likely to lead to variation in layer thickness. To view more detail, the sample is bent to produce delamination and cracks in the sample. These cracks are used view the structure of the sample from the roots i.e., growing from the copper substrate. This is shown in figure 4.9.

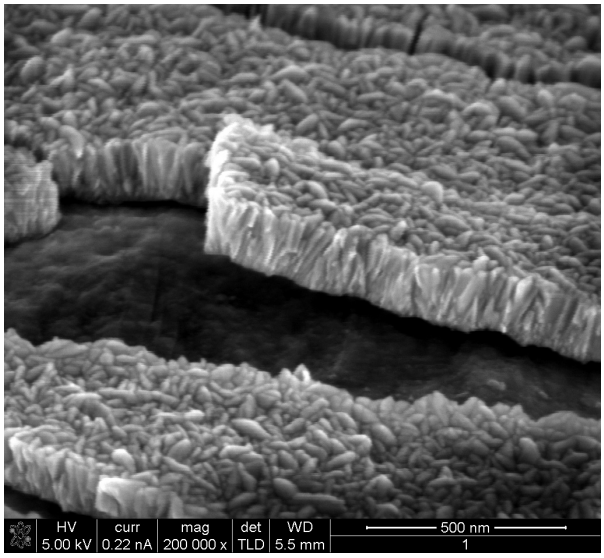

Figure 4.9: View through a fissure created by bending the film

To approximately determine the layer thickness, the built-in measurement function in the SEM apparatus is used. The variation in thickness across the surface can be seen more clearly in figure 4.10.

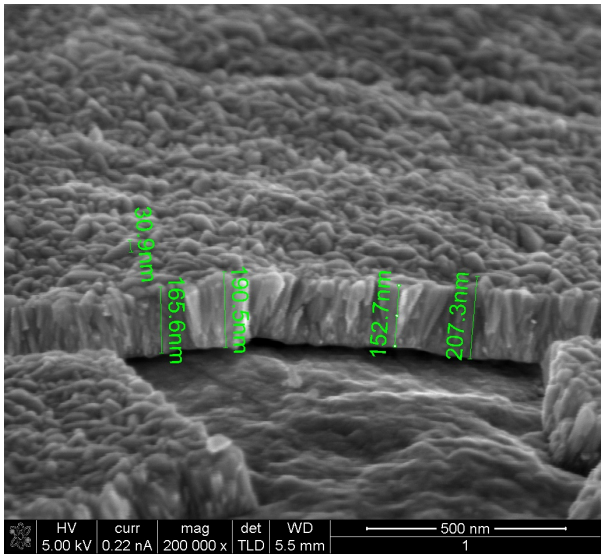

Figure 4.10: Approximate layer thickness measurements across the fissure

We see here that the layer thickness is fairly uniform, around $160nm$. But, there is a large degree of variation due to the unevenness of the top layer. This can viewed using the size of the a nodule on the top surface, which is about $30nm$ thick.

To verify the elemental composition of the layer, EDX was performed on the sample. The results are shown in figure 4.11. We see that the Zn and O are approximately stoichiometric and thus we can confirm that the deposition met the goal of forming a ZnO layer on the substrate. It is possible that some of the oxygen is in form of oxidised copper, and therefore the layer is not entirely stoichiometric.

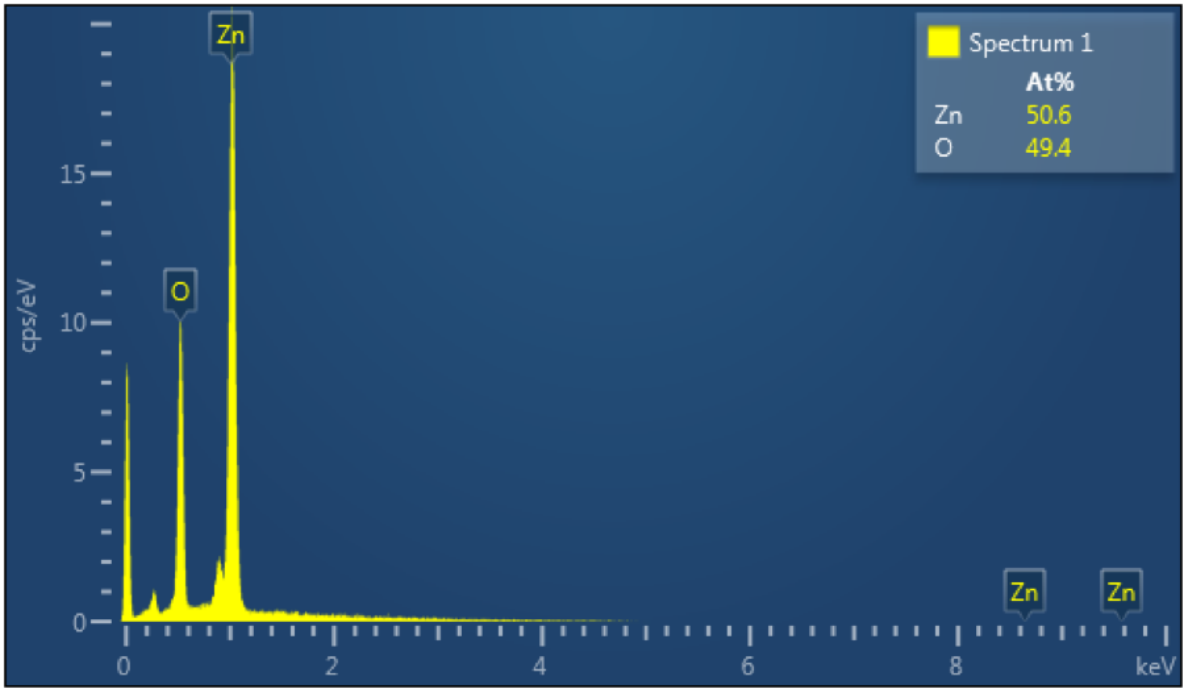

Figure 4.11: EDX results for the ZnO layer

4.4. Li Plating/Stripping Behaviour

The results of the Li plating/stripping tests are discussed below. The voltage/time charts are used to provide an indication of the reactions occurring and to examine what the causes of observed over-potentials might be. These results are correlated with the capacity/cycles charts, which display sharp changes corresponding to variations in plating/stripping behaviour. The results are categorised into 4 current densities: 1, 5 and $10 mA/cm^2$. The typical current densities in commercial cells are in the range of 0.5 - $2 mA/cm^2$. Higher current densities are being investigated because they could still provide insight into the fundamental nature of the reactions taking place, and deliver results in shorter times. The voltage/time charts are split in halves for better readability.

4.4.1. Current density: $1 mA/cm^2$

The voltage/time charts for bare copper and ZnO on copper at $1 mA/cm^2$ are shown in figures 4.12 and 4.13. The black lines represent the cell with ZnO and the red lines represent the cell with bare copper.

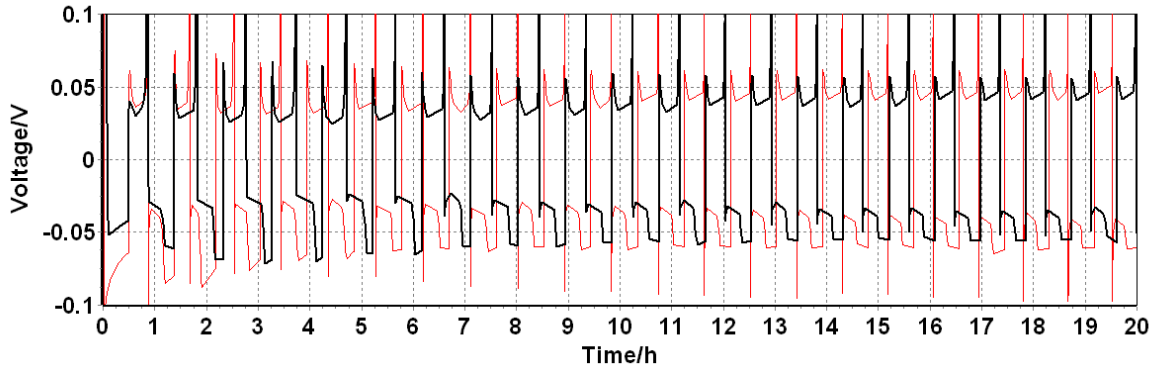

Figure 4.12: Voltage v/s time at $1 mA/cm^2$: 1st half

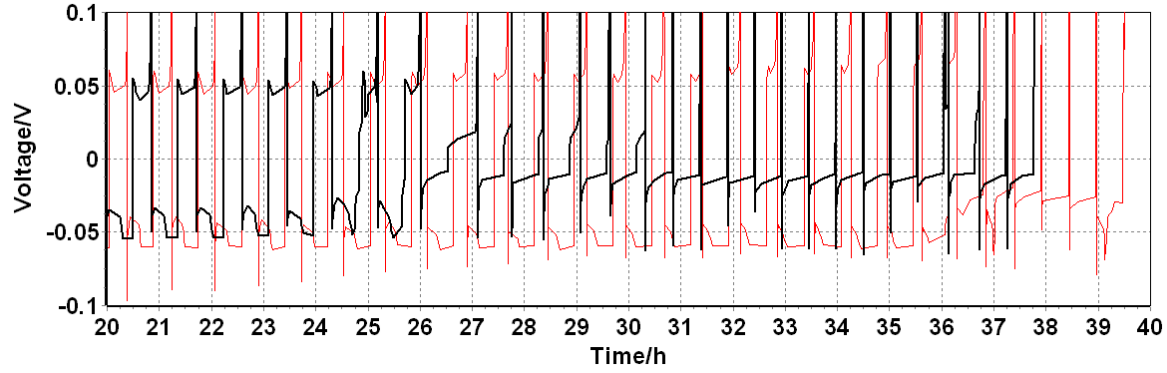

Figure 4.13: Voltage v/s time at $1 mA/cm^2$: 2nd half

The following characteristics are seen:

1. **The first discharge plateaus are very different**
   - The discharge plateau for ZnO is observed at around $-0.05V$ v/s $-0.1V$ for copper
   - The plateaus begin to coincide after 3 hours
2. **There are consistently higher plating overpotentials for bare copper than for** ZnO

- The overpotentials likely indicate the formation of Li nucleation sites
- The discharge curves sinks to $-0.1V$ in nearly every discharge cycle before recovering to the plateau at around $-0.05V$
- The overpotentials appear to grow smaller after around 23 hours

3. **The stripping overpotentials are similar for both materials**
   - The stripping plateau occurs at about $0.05V$ in both cells
   - The plateaus begin to decrease in size before collapsing
   - The collapse of the plateaus likely indicates the beginning of dendrite formation, from which Li cannot be recovered

The corresponding capacity/time charts for bare copper and ZnO on copper are shown in figure 4.14. The upward triangles represent stripping capacities (ZnO - black; copper - red). The downward triangles represent plating capacities (ZnO - green; copper - blue).

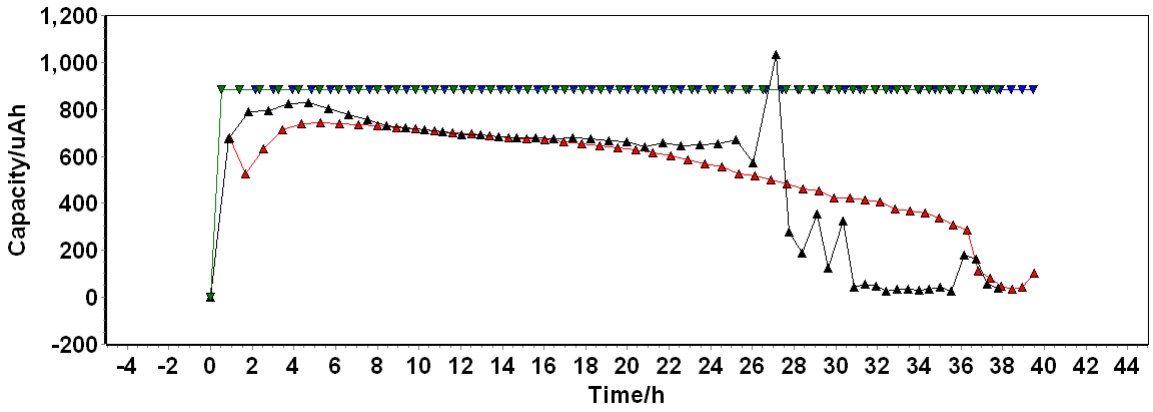

Figure 4.14: Capacity deterioration over 50 cycles for Li plating/stripping at $1mA/cm^2$

The following can be observed and inferred:

1. **The stripping/plating efficiencies appear to be higher initially for** ZnO
   - This suggests that more of the Li that is plated can be reversibly recovered
   - This only last for a few cycles before dropping in performance
2. **The drop in performance is much more gradual for copper than for** ZnO
   - The performance with ZnO drops sharply after about 25 hours
   - The deterioration began earlier for copper, but the cell lasted longer eventually

4.4.2. Current density: $5mA/cm^2$

The voltage/time charts at $5mA/cm^2$ are shown in figures 4.15 and 4.16.

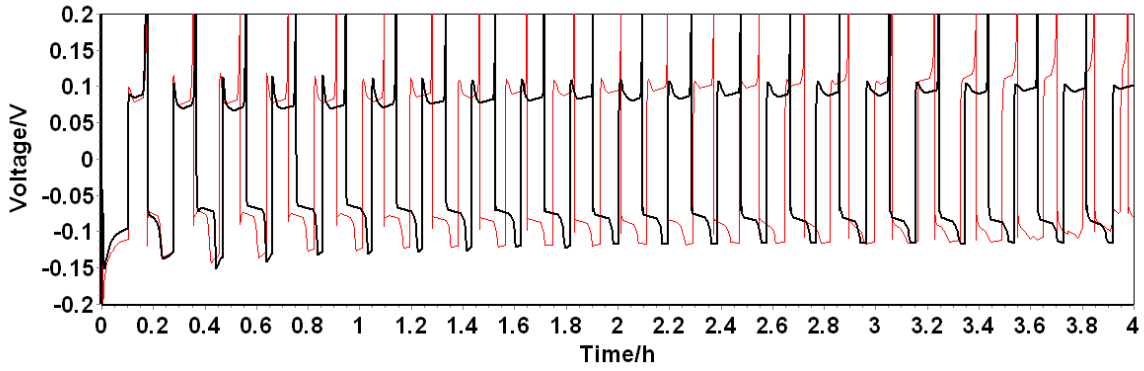

Figure 4.15: Voltage v/s time at $5mA/cm^2$: 1st half

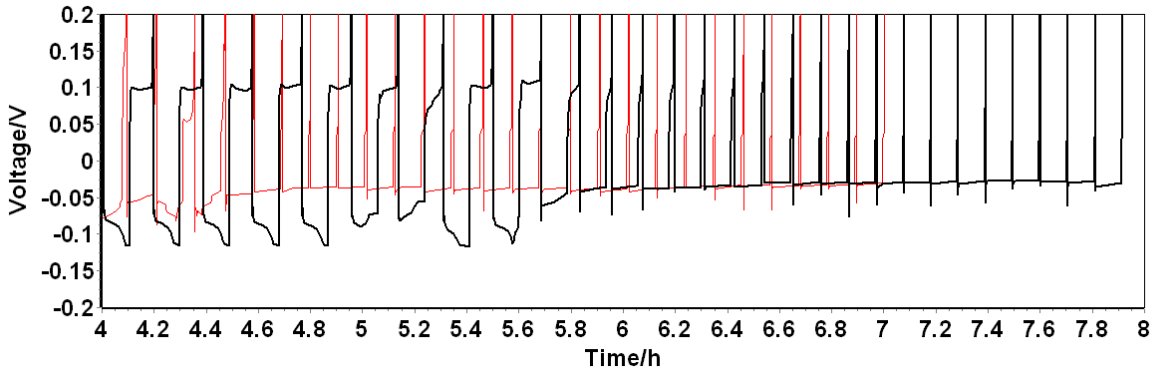

Figure 4.16: Voltage v/s time at $1mA/cm^2$: 2nd half

The following characteristics are seen:

1. **The performance of bare copper and ZnO seem comparable initially**
   - The performance of the bare copper cell fades earlier than the ZnO cell
   - The discharge plateaus actually appear to grow wider after around 4 hours
2. **The lower plating plateau disappears after 5 hours in the ZnO cell**
   - This plateau occur at a slightly lower potential
   - As the cells fail, the discharge plateaus coincide

The corresponding capacity/cycle charts for bare copper and ZnO on copper are shown in figure 4.17.

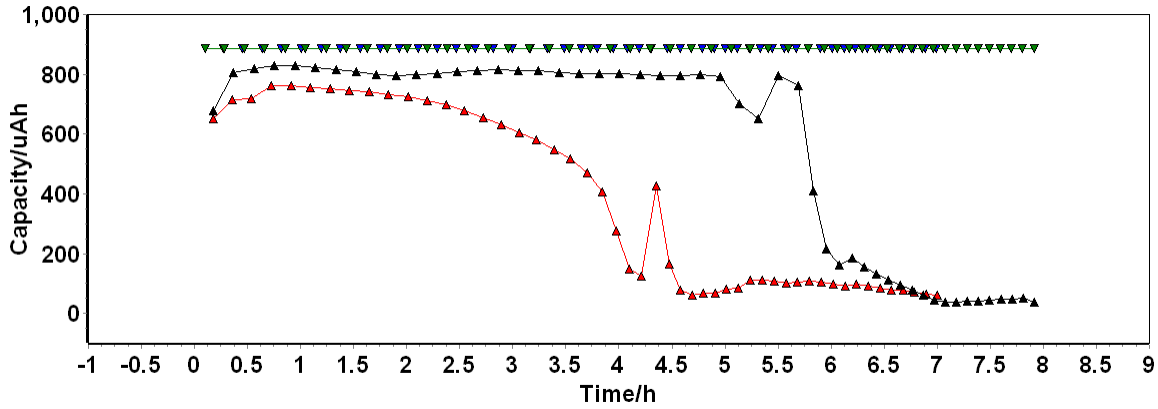

Figure 4.17: Capacity deterioration over 50 cycles for Li plating/stripping at $5mA/cm^2$

The following can be observed and inferred:

1. **The ZnO cell shows better performance than the bare copper cell**

   - The performance is only equal at the 1st cycle
   - The performance of the ZnO cells is consistent until cell failure

2. **The performance drop is again sharp in the ZnO cell**

   - The ZnO cell fails immediately after 5.5 hours
   - The performance of the copper cell gradually fades after 2 hours before failing at the 4.5 hour mark

4.4.3. Current density: 10 mA/cm^2

The voltage/time charts at $10mA/cm^2$ are shown in figures 4.18 and 4.19.

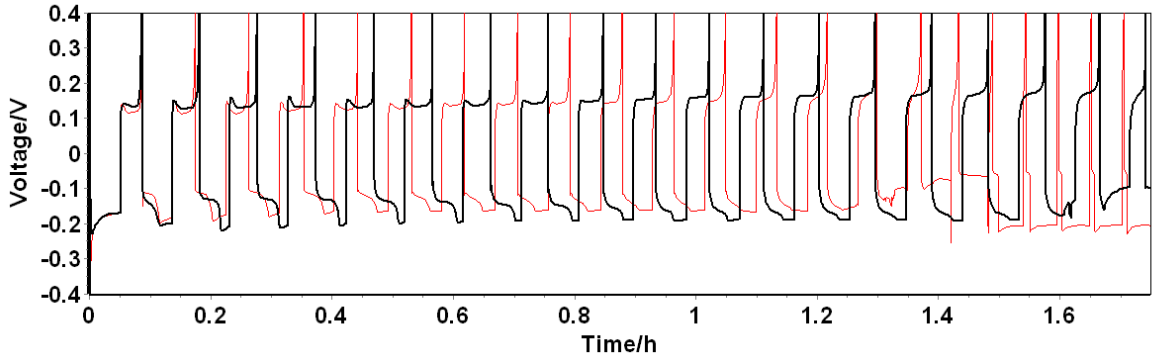

Figure 4.18: Voltage v/s time at $10mA/cm^2$: 1st half

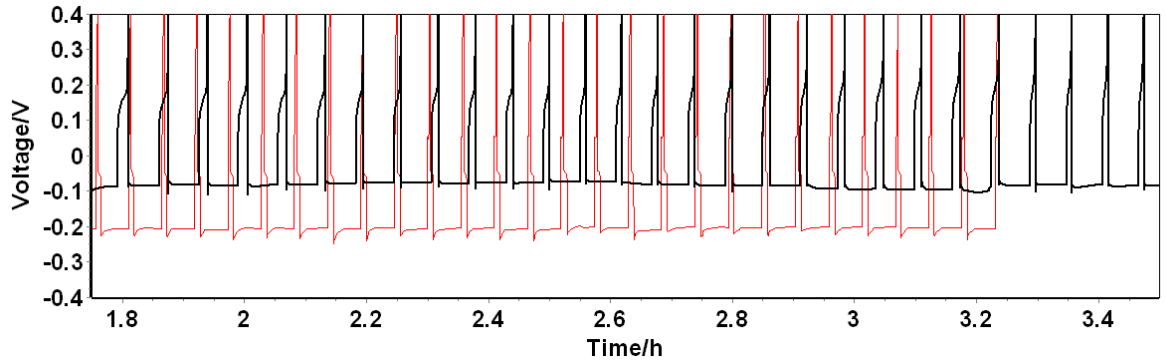

Figure 4.19: Voltage v/s time at $10mA/cm^2$: 2nd half

The following characteristics are seen:

1. **The discharge plateau of the ZnO cmoves up after 1.6 hours**
   - The plateau is initially at $-0.2V$ and then moves to $-0.1V$
   - This indicates that a different kind of reaction is taking place
2. **One of the discharge plateaus for the copper cell collapses after 1.4 hours**
   - The plateau at $-0.1V$ is lost and only the one at $-0.2V$ remains
   - This is preceded by a sharp overpotential that did not occur in previous cycles

The corresponding capacity/cycle charts for bare copper and ZnO on copper are shown in figure 4.20.

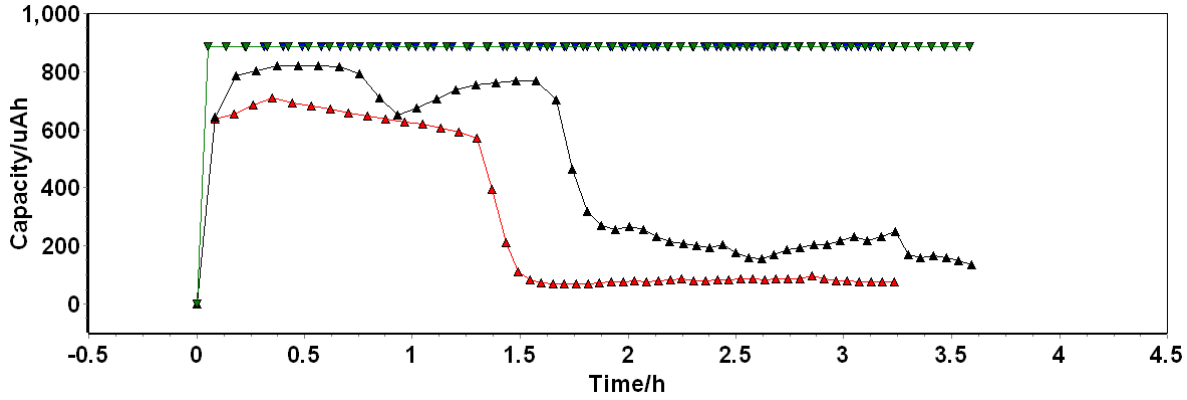

Figure 4.20: Capacity deterioration over 50 cycles for Li plating/stripping at $10mA/cm^2$

The following can be observed and inferred:

1. **The ZnO cell fails much later than copper cell**
   - But, there is drop in both plating and stripping capacities in the 0.5 - 1 hour window
   - The plating and stripping capacities coincide in this range
2. **There is a large gap in efficiencies at this current density**
   - Aside from the aforementioned window, the ZnO has a much higher efficiency that the copper cell
   - The copper cell again has a slightly more gradual performance descent

5

Conclusions & Recommendations

This chapter contains a short summary of the results from the thesis project. The research questions asked in the 1st chapter will be addressed again to see how far they have been answered. Based on these results, recommendations for future work will also be made.

5.1. Polymer Electrolyte

The thesis concluded with the successful development of a thin film polymer electrolyte. The parameters determined to be ideal for the synthesis are listed in table table 5.1:

Polymer	PEO ($600K$ mol wt.)
Salt	$LiTFSI$
$EO:Li$	$20:1$
Solvent	ACN
Solvent weight ratio	90%
Solution stirring time/temp	$2h/60°C$
Casting substrate	PTFE
Casting method	Blade casting
Wet film thickness	$1500\mu m$
Film drying time/temp	$24h/R.T.$ (argon) + $48h/60°C$ (vacuum)
Dry film thickness	$80-100\mu m$

Table 5.1: Final parameters for polymer electrolyte synthesis

The measured properties of the developed polymer electrolyte are listed in table 5.2:

Conductivity ($60°C$)	$3x10^{-6}$
Conductivity ($25°C$)	$3x10^{-4}$
Conduction Model	Vogel-Tamann-Fulcher (VTF)
Conductivity v/s Pressure	No clear relationship
Transference Number	0.21

Table 5.2: Measured properties of developed polymer electrolyte

The development of the polymer electrolyte has already progressed further under Dr.Ming Liu at TU Delft, with the successful use of the plasticiser succinonitrile (SN). The use of Differential Scanning Calorimetry (DSC) to investigate the differences in glass transitions between the polymer electrolyte with and without the plasticiser would help us to understand what structural changes have occurred.

Further, the use of the polymer electrolyte in similar Li plating/stripping experiments would help to understand the gap that remains to be filled between liquid and polymer electrolytes.

5.2. Interfacial Layer

The chosen material for the interfacial layer was ZnO. It was deposited on a copper substrate using Atomic Layer Deposition (ALD). The effects of the layer on Li plating/stripping performance were investigated at different current densities for a fixed amount of deposited Li. The results are summarised in 5.3.

Current Density (mA/cm^2)	**Effect of ZnO Layer**
1	1. Delayed dendrite formation (30 cycles v/s 5 cycles) 2. Higher plating plateau ($-0.05V$ v/s $-0.1V$) 3. Higher plating/stripping efficiency before dendrite formation
5	1. Again, delayed dendrite formation (25 cycles v/s 5 cycles) 2. Delayed failure of ZnO cell (32 cycles v/s 27 cycles) 3. Performance is still superior with ZnO
10	1. Delayed dendrite formation (28 cycles v/s 5 cycles) 2. Delayed failure of ZnO cell (32 cycles v/s 17 cycles) 3. Higher plating/stripping performance

Table 5.3: Effects of ZnO on Li plating/stripping at different current densities

We can conclude that the ZnO may provide improved plating performance. But, we still have no conclusions about why may be. The next steps need to directed towards understanding the phenomena occurring at the surface of the ZnO layer. Thus, either in-situ or ex-situ analysis using XRD, XPS etc. would be beneficial in understanding the chemical and structural changes. This can be studied at: (1) different current densities (2) different cycling ages.

5.3. Answers to Research Questions

1. **What type of polymer electrolyte could have the requisite mechanical, electrical and chemical properties?**
   - Thin film PEO-LiTFSI electrolyte
   - It is mechanically strong and chemically stable
   - But, electrical conductivity is low at room temperature
2. **How do you develop this electrolyte in a scalable, reproducible manner?**
   - Wet blade casting using acetonitrile as solvent
   - Dry under argon at $25°C$ and then under vacuum at $60°C$
3. **How does the developed electrolyte behave electrochemically under different operating conditions?**
   - No significant effects of pressure on performance
   - Time of equilibriation at a given temperature is critical, especially around $50°C$
4. **What type of interfacial layer could aid the Li plating/stripping process?**
   - Thin layer of ZnO nanoparticles
   - Reversible Zn-Li alloying process is key
5. **How can this interfacial layer be developed?**
   - Spatial Atomic Layer Deposition (s-ALD)

- Tested thickness of $\sim 200nm$

6. **How does the performance of the layer change under different operating conditions?**
   - Effect of layer appears to be more significant at higher current densities
   - Performance is consistent but failure occurs in a sudden fashion
7. **Does this layer achieve the aim of improving the plating/stripping performance?**
   - Yes, it appears so based on initial results
   - Further investigations on surface characteristics are required

A

Appendix A: Thermal Pre-treatment of Polymer Electrolyte

In the current procedure, the polymer electrolyte is pre-treated at $60°C$ for 24 hours prior to testing. We tested other temperatures and times but these conditions were found to give the most consistent results. To investigate the effect of pre-treatment, we also used a temperature of $70°C$. The results over a period of multiple days are shown below, and compared to those are $60°C$. A sharp departure from expected conductivity values is visible after around 24 hours at $70°C$. The likely cause is the melting of the polymer, which increases the wettability of the interfaces. This is therefore not likely to be a reflection of bulk ionic conductivity.

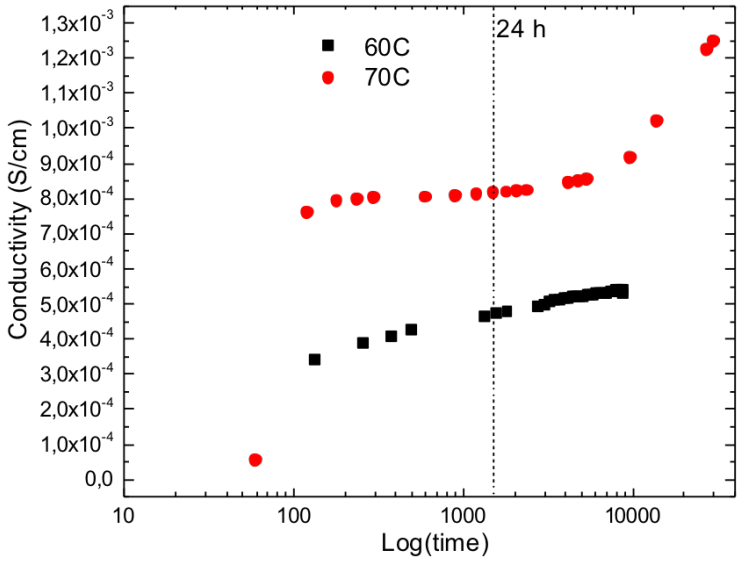

Figure A.1: Effect of thermal pre-treatment on the electrolyte

B

Appendix B: XRD Spectrum of ZnO Layer

We attempted to further to investigate the crystalline structure of the ZnO layer using XRD. But the characteristic peaks of ZnO [32] were not visible. This is likely because the layer thickness was too small and the spectrum was dominated by the copper peak. Further refinement is required to confirm the results. The XRD spectrum as recorded is shown in B.1.

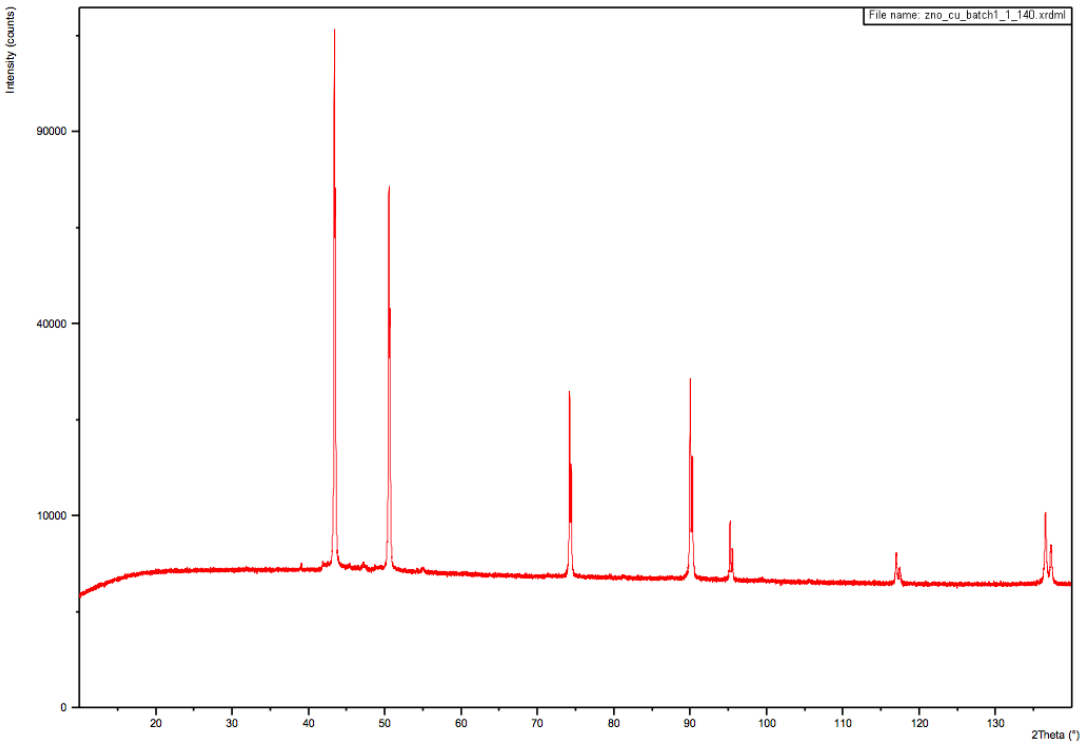

Figure B.1: XRD spectrum of the ZnO deposited on copper

Bibliography

[1] U. of Tokyo, *Fuel cell/battery system,* (2018).

[2] M. Osiak, H. Geany, E. Armstrong, and C. O'Dwyer, *Structuring materials for lithium-ion batteries: advancements in nanomaterial structure, composition, and defined assembly on cell performance,* Journal of Materials Chemistry **2**, 9433 (2014).

[3] C. Reports, *Samsung investigation reveals new details about note 7 battery failures,* (2017).

[4] S. Gallagher, *Ntsb blames bad battery design—and bad management—in boeing 787 fires,* (2014).

[5] P. Bai, J. Li, F. R. Brushetta, and M. Z. Bazant, *Transition of lithium growth mechanisms in liquid electrolytes,* Energy & Environmental Science **9**, 3221 (2016).

[6] G. Bieker, M. Winter, and P. Bieker, *Electrochemical in situ investigations of sei and dendrite formation on the lithium metal anode,* Physical Chemistry and Chemical Physics **17**, 8670 (2015).

[7] X.-B. Cheng, R. Zhang, and C. zi Zhao, *Toward safe lithium metal anode in rechargeable batteries: A review,* Chemical Reviews: American Chemical Society **117**, 10403 (2017).

[8] Z. Xue, D. Heb, and X. Xie, *Poly(ethylene oxide)-based electrolytes for lithium- ion batteries,* Journal of Materials Chemistry **3**, 19218 (2015).

[9] Y. Liu, D. Lin, Z. Liang, J. Zhao, K. Yan1, and Y. Cui, *Lithium-coated polymeric matrix as a minimum volume-change and dendrite-free lithium metal anode,* Nature Communications **7** (2016), 10.1038/ncomms10992.

[10] Z.-W. Fu, F. Huang, Y. Zhang, Y. Chu, and Q.-Z. Qin, *The electrochemical reaction of zno thin films with lithium,* Journal of the Electrochemical Society **150**, A714 (2003).

[11] Gamry, *Basics of electrochemical impedance spectroscopy,* (2018).

[12] K. Gelderman, L. Lee, and S. W. Donne, *Flat-band potential of a semiconductor: Using the mott–schottky equation,* Journal of Chemical Education **84**, 685 (2007).

[13] M. Marzantowicz, J. Dygas, and F. Krok, *Impedance of interface between peo:litfsi polymer electrolyte and blocking electrodes,* Electrochimica Acta **53**, 7417 (2008).

[14] S. Zugmanna, M. Fleischmann, M. Amerellera, R. Gschwind, H. Wiemhöfer, and H. Gores, *Measurement of transference numbers for lithium ion electrolytes via four different methods, a comparative study,* Electrochimica Acta **56**, 3926 (2011).

[15] A. Illiberi, F. Roozeboom†, and P. Poodt, *The electrochemical reaction of zno thin films with lithium,* ACS Applied Materials and Interfaces **150**, A714 (2003).

[16] A. Casimir, O. O. Hanguang Zhang, J. C. Amine, and G. W. Jun Lu, *Silicon-based anodes for lithium-ion batteries: Effectiveness of materials synthesis and electrode preparation,* Nano Energy **27**, 2211 (2016).

[17] B. Insider, *Samsung announces what caused the galaxy note 7 to overheat and explode,* (2017).

[18] J. W. Fergus, *Ceramic and polymeric solid electrolytes for lithium-ion batteries,* Journal of Power Sources **195**, 4554 (2010).

[19] K. M. Diederichsen, H. G. Buss, and B. D. McCloskey, *The compensation effect in the vogel–tammann–fulcher (vtf) equation for polymer-based electrolytes,* Macromolecules **50**, 3831 (2007).

[20] S. B.Aziza, T. J.Woo, M. F. Z. Kadir, and H. M. Ahmed, *A conceptual review on polymer electrolytes and ion transport models,* Journal of Science: Advanced Materials and Devices **3**, 1 (2018).

[21] G. K. Kiran, T. R. Penki, N. Munichandriah, and P. V. Kamath, *Electrochemical impedance studies of capacity fading of electrodeposited zno conversion anodes in li-ion battery,* Bulletin of Materials Science **40**, 427 (2017).

[22] P. Bruce, J. Evans, and C. A. Vincent, *Conductivity and transference number measurements on polymer electrolytes,* Solid State Ionics **28**, 918 (1987).

[23] P. Bruce, J. Evans, and C. A. Vincent, *Electrochemical measurement of transference numbers in polymer electrolytes,* Polymer **28** (1987).

[24] S. Swapp, *Scanning electron microscopy (sem),* (2018).

[25] D. Henry, *Electron-sample interactions,* (2018).

[26] N. P. A. Services, *Sem-edx,* (2018).

[27] B. L. Dutrow and C. M. Clark, *X-ray powder diffraction (xrd),* (2018).

[28] D. Henry, N. Eby, J. Goodge, and D. Mogk, *X-ray reflection in accordance with bragg's law,* (2018).

[29] P. A. O'Connella and G. B. McKennab, *Arrhenius-type temperature dependence of the segmental relaxation below tg,* Journal of Chemical Physics **110** (1999).

[30] S. Seki, M. A. B. H. Susan, T. Kaneko, A. N. Hiroyuki Tokuda, and M. Watanabe, *Distinct difference in ionic transport behavior in polymer electrolytes depending on the matrix polymers and incorporated salts,* Journal of Physical Chemistry **109**, 3886 (2005).

[31] H. Dai and T. A. Zawodzinski, *The dependence of lithium transference numbers on temperature, salt concentration and anion type in poly (vinylidene fluoride)– hexafluoropropylene copolymer-based gel electrolytes,* Journal of Electroanalytical Chemistry **459**, 111 (1998).

[32] S. Talam, S. R. Karumuri, and N. Gunnam, *Synthesis, characterization, and spectroscopic properties of zno nanoparticles,* ISRN Nanotechnology (2012), http://dx.doi.org/10.5402/2012/372505.